https://dx.doi.org/10.1016/j.oceaneng.2020.107577

Modelling of suction bucket foundation in clay: from finite element analyses to macro-elements

Zhen-Yu YIN[1,*], Jing-Cheng TENG[1,2], Zheng LI[3] and Yuan-Yuan ZHENG[4]

Affiliation
1 Department of Civil and Environmental Engineering, The Hong Kong Polytechnic University, Hung Hom, Kowloon, Hong Kong, China
2 Southern Marine Science and Engineering Guangdong Laboratory (Guangzhou), 1119 Haibin Rd., Nansha District, Guangzhou, China
3 IFSTTAR, GERS, GMG, Bouguenais, France
4 School of Civil Engineering, SUN Yat-Sen University, Zhuhai, China
* Corresponding author: Dr Zhen-Yu YIN, Tel: +852 3400 8470; Fax: +852 2334 6389;
E-mail: zhenyu.yin@polyu.edu.hk; zhenyu.yin@gmail.com

Abstract: This study aims at modelling the suction bucket foundation in clay from full finite element analyses to simplified macro-element. To ensure the reliability of finite element simulation results as much as possible, two well-known constitutive models, the Modified Cam-Clay model (MCC) and the Hardening Soil model (HS), are adopted respectively for the foundation soil which is normally consolidated clay with parameters directly determined from laboratory tests instead of inverse analysis or fitting using simple models in previous studies. The finite element analyses using both models are validated by comparing centrifugal tests and further extended to study the failure patterns in V–H–M (**V**ertical force–**H**orizontal force–**M**oment) space through radial displacement tests. Based on all results, two new alternative analytical formulations based on both models are then proposed to describe the three-dimensional (3D) failure envelope in V–H–M space. Finally, two new alternative macro-element design models of suction bucket foundation in clay under the same framework of hypoplasticity for both monotonic and cyclic loading conditions are proposed. By comparing with experimental results, the effectiveness and efficiency of both macro-element models are verified applicable and the one based on HS has slightly better performance than the one of MCC.

Keywords: suction bucket foundation; failure envelope; clay; finite element method; cyclic loading; macro-element

1 Introduction

A suction bucket is a closed-top steel tube that is lowered to the ocean floor, allowing sediments to seep in under their own weight. Water is then pulled out of its interior to produce a suction force that pushes it to full depth. The main advantages of a suction bucket foundation are its adaptability to various seabed depths, ease of installation, reusability and ability to mobilise tremendous passive suction during uplift (Zhang *et al*., 2013). Suction bucket foundations often need to bear long-term loads. Vertical force, horizontal force and bending moment can be transferred to the bucket foundation under the upper building, which is defined as the combined loading mode.

To optimise their design, however, it is necessary to understand the performance of the suction bucket foundation. A great deal of experimental investigation has addressed the response of foundations under general monotonic/cyclic combined loads, which can be classified as: (1) prototype and reduced-scale field tests, e.g., Tjelta (1994), Houlsby *et al*. (2005), Barari and Ibsen (2011, 2012), Zhang *et al*. (2015); (2) scaled 1-g model test, e.g. Kelly *et al*. (2006), Villalobos *et al*. (2010), Guo *et al*. (2012); (3) centrifuge tests, e.g. Fuglsang and Steensen-Bach (1991); Renzi *et al*. (1991) ; Allersma *et al*. (1999); Cao (2003); Cao *et al*. (2004); Zhang *et al*. (2003); Raines and Garnier (2008); Kim *et al*. (2005); Clukey *et al*. (1995); Watson and Randolph (1997); Cassidy *et al*. (2006); Lu *et al*. (2007); Zhang *et al*. (2007); Kim *et al*. (2014). Note that this study focuses primarily on suction bucket foundations in clay.

Experimental studies are valuable and provide basis for the design, but it is time-consuming and costly to study failure envelope and the characteristics of bearing capacity using a model test. Greater time savings and economies can be had using the finite element method (FEM). Many researchers have numerically studied the behaviour of a suction bucket foundation in clay, including the characteristics of vertical bearing capacity under installation (Gerolymos *et al*., 2015; Harireche *et al*., 2013; Kourkoulis *et al*., 2014; Muduli *et al*., 2013; Samui *et al*., 2011; Zhou and Randolph, 2006) and bearing capacity behaviours under general loads (Cheng *et al*., 2016; Gourvenec and Randolph, 2003; Randolph and House, 2002; Skau *et al*., 2018; Vásquez *et al*., 2010; Zdravkovic *et al*., 1998; Zdravković *et al*., 2001). A variety of constitutive models are used to study the response of suction bucket foundations under combined loads. However, many studies used typical profile of soil strength or inverse calculation methods of empirical equation to calibrate the model parameters (Zhang *et al*.,

2020). Since the reliability of numerical simulation largely depends on whether the results of FEM can correctly regenerate the nonlinear response of soil, soil parameters directly from conventional laboratory tests representing nonlinear soil behaviour instead of only indirectly from site investigation or inverse analysis should be recommended, as tried in this study.

FEM allows applications using complex constitutive laws, 3D meshes and combined loads. However, these incur huge costs of data storage capacity and computer memory, requiring the use of high-performance computing machines and large amounts of time (Zhang *et al.*, 2019). In addition, professional engineers must first become comfortable using the model. Accordingly, a new method called the macro-element method is proposed which is a generalised 2D or 3D force-resultant model. This method centralises the behaviour of the foundation and soil system to a point. For example, a hyperplastic model was adopted and used on suction bucket foundations by Nguyen-Sy and Houlsby (2005). Similarly, Di Prisco *et al.* (2003a, 2003b, 2006) and Foglia *et al*. (2015) conducted a series of laboratory tests on suction bucket foundations in sand under monotonic and cyclic loads, interpreting the results of the tests with the macro-element method, using the existing analysis model of Villalobos *et al*. (2009), with appropriate modifications to accommodate cyclic loading of the foundation and applications. Skau *et al*. (2018) analysed the characteristic behaviour of suction bucket foundations under irregular cyclic loads using a multi-surface plasticity framework. Most recently, Jin *et al*. (2019) proposed a hypoplastic macro-element model for suction bucket foundation in sand under drained condition with good performance and easy implementation. It thus would be nice to follow this framework to propose a simple design tool for suction bucket foundation in clay.

Therefore, in this paper the failure patterns of suction bucket foundation in clay are first studied by FEM simulations. The numerical analyses are verified using centrifugal tests of suction bucket foundation in a normally consolidated kaolin clay, followed by selecting a more representative loading combinations to reproduce the failure patterns under undrained condition. The modified Cam-Clay model (MCC) and Hardening Soil model (HS) are adopted for clay respectively to ensure the reliability of simulation results as much as possible. As a basis, two alternative failure envelops based on MCC and HS in *V-H–M* space are proposed and compared. Then, two novel alternative macro-element models are developed under the same framework of hypoplasticity using the two proposed failure envelops respectively. Through two monotonic and two cyclic model tests, the predictive

ability of two hypoplastic macro-element models is evaluated and compared.

2 Numerical simulation

In this section, the numerical modelling of suction bucket foundation in clay is introduced. Simulations using a commercial finite element code PLAXIS-3D are first validated using centrifuge tests of a suction bucket foundation of Watson (1999).

2.1 Adopted experimental campaign

A series of laboratory tests of a suction bucket foundation in a normally consolidated Kaolin clay are well documented, including centrifuge tests and application of monotonic loadings selected hereafter (Watson, 1999). The centrifuge at the University of Western Australia has a sample dimensions of 390 mm × 650 mm × 325 mm high, which at 200 g represents a sample bed up to 78 m × 130 m × 65 m. The suction bucket is based on a steel structure having a diameter of 50 mm, 150 mm long with a skirt thickness of 1 mm. The suction bucket foundation was used to perform one undrained bearing capacity test and two sideswipe tests.

2.2 Finite element model

The numerical model of the suction bucket foundation was modelled according to the size and shape of the foundation in prototype scale (78 m × 130 m × 65 m). Plane strain condition was assumed in finite-element analysis utilising axial symmetry, shown in Figure 1. The horizontal displacements are constrained on the lateral sides. Both vertical and horizontal displacements are constrained on the bottom. The finite-element mesh was constituted of 19664 10-noded tetrahedron elements resulting in 30098 nodes. Mesh-sensitivity studies were done to ensure that the mesh was dense enough to produce accurate results.

According to Watson (1999), the values of parameters of MCC model for the normally consolidated Kaolin clay are listed in Table 1. Note that a typical value of Poisson's ratio for clays ($\nu = 0.3$) was given for simulations since no value was not provided by Watson (1999). For HS model, the parameters were equivalently determined using the equations by Schanz *et al*. (1999):

- power of stress dependency for clay m = 1;

- reference oedometric modulus $E_{oed}^{ref} = p^{ref} / \lambda^* = 816.6 \text{ kN/m}^2$ (with $\lambda^*=\lambda/(1+e_0)$);

- reference secant modulus $E_{50}^{ref} = 1.25 E_{oed}^{ref} = 1026.7 \text{ kN/m}^2$;

- reference unloading/reloading modulus $E_{ur}^{ref} \approx p^{ref} / \kappa^* = 15133.3 \text{ kN/m}^2$ (with $\kappa^*=\kappa/(1+e_0)$).

The model for the suction bucket is built using PLAXIS-3D, shown in Figure 1. The aspect ratio (L/D ratio) is equal to 0.5, with D = 7.5 m. The bucket foundation is composed of two rigid body elements, the bucket lid and the skirt, with a reference point for both at the symmetry line (centre) of the foundation. After the bucket foundation model is constructed, the boundary conditions of this structure were applied, as summarised in Table 2 for the translation and rotation conditions defined in PLAXIS. The interfaces of the skirt and the lid of suction bucket are created to allow proper modelling of the interaction between soil and structure. The interface is set to the rigid Coulomb friction model for the entire simulation with a friction angle of 10.7° (= 1/2*ϕ_c: half of critical friction angle of the soil).

The initial stress state of the foundation soil was generated according to the gravity of saturated unit weight of the Kaolin clay (γ_{sat} = 16.5 kN/m^3). The coefficient of earth pressure at rest is set as $K_{nc}^0 = 1 - sin\phi_c = 0.64$ according to Jacky's formula. The installation of suction bucket into foundation soil is ignored, since this effects very locally the soils surrounding the bucket and thus gives very slight influence according to Jin *et al*. (2019). Furthermore, since the Kaolin clay has very low permeability, all simulations were carried out under full undrained condition.

2.3 Validation against centrifuge tests

Three centrifuge tests of Watson (1999) presented in Table 3 were simulated. The sideswipe tests are subjected to a constant vertical load *V = 0* and *V = V'* respectively. Both tests are subjected to horizontal displacement at the loading reference point of the suction bucket. Figure 2 shows the result of K1-1 (pure penetration test) test, which applied *z* (vertical displacement) versus *V* (vertical force) to compare the results obtained from the numerical simulations by using the MCC and HS respectively. The simulation result of the MCC model is slightly closer to the experimental result than that of the HS model. Figure 3 shows comparisons of experimental and simulated results for K1-2 and K1-3. Both results by the MCC model and HS model agree with experimental results with almost the same

performance. Although there are discrepancies between experimental and numerical results, all simulation results for different paths together should be acceptable.

3 Numerical investigation of the failure envelope in the *H–M-V* space

3.1 Failure envelope in the *H–M* plane

Gottardi *et al*. (1999) presented two displacement control paths to determine the failure envelope of the suction bucket foundation: (1) *Swipe tests:* Firstly, a certain level of vertical load is applied to the foundation, after which a large horizontal displacement (maximum load principle) is applied to obtain H_R (horizontal resistance) under this constant vertical load. (2) *Radial displacement tests:* The increment or decrement of the ratio between the horizontal displacement and rotation–displacement remains unchanged.

In this study, the radial displacement control method is used as the main method. The symbols of loads (*V–H–M*) are applied on the *LRP* (loading reference point) of the suction bucket foundation, as shown in Figure 4. The outer diameter (D) and skirt length (L) of the model are 7.5 m and 3.75 m, respectively. The purpose of this research is to evaluate the bearing capacity of this suction bucket foundation without discretisation of possible upper buildings.

The mass of typical offshore wind turbine is around 600 tons, which is relatively light (vertical deadload 6 MN). As a result, the design of the horizontal and rotational bearing capacities is critical. To study the failure surface form in the *H–M* plane, a constant radial loading ratio is determined and the different displacements applied on the LRP of the suction bucket foundation. As shown in Figure 5, a certain vertical load was applied to a designated value $\chi = V_i/V_0$ (V_0 is maximum vertical load) and the radial displacement tests are then conducted. The displacement should be large enough to ensure that maximum capacity is reached. ($\chi = 0$ means that only the self-weight of suction bucket is considered.)

Figure 6 shows the selection method for determining the bearing capacity: the ends of the loading paths up to failure of the foundation determine the ultimate bearing capacity, and the lines before the ends represent loading paths with different ratios between the horizontal displacement and rotation angle (i.e. dash line for higher rotation and solid line for higher displacement). Examples of the *H–M* plane obtained by numerical radial displacement test

simulation are presented in Figure 7. The increment or decrement of the ratio between the horizontal displacement u and rotation–displacement θ is constant ($\delta\theta/\delta u \equiv$ constant). The failure envelope is obtained by the superposition of various failure points, as presented in Figure 7(a), and for different vertical load levels, as shown in Figures 7(b).

From Figure 7, some results of the failure surface can be summarised as follows: (1) the bending moment has a noticeable impact on the horizontal bearing capacity that depends on the loading direction; (2) the shape of the failure envelope of a suction bucket foundation in clay is the inclined ellipse; (3) with an increase in the pre-loaded vertical load, the size of the failure envelope decreases.

3.2 Impact of vertical loads on the H–M failure envelope

The bearing capacity in the *H–M* plane of the suction bucket foundations changed remarkably under different values of vertical loading. To quantify this impact, a procedure similar with section 3.1 is used hereafter. Specifically, numerical simulation of radial displacement tests under different vertical loads are conducted. The failure envelopes under different vertical loads are presented in Figure 7(b). Figure 7(a) also show the field case (χ = 0). Overall, the following conclusions can be drawn: (1) the impact on the inclination degree of failure envelope under different vertical loads can be ignored; (2) the size of the failure envelope decreases with a rise in the value of the vertical load.

3.3 Impact of vertical loads on the H–V failure envelope

Several numerical swipe tests under different levels of vertical load are carried out to determine the failure envelope of the *H–V* plane. A series of constant vertical loads are applied on the LRP of the suction bucket foundation and the maximum load principle (see section 3.1) is again used to obtain the failure locus; see Figure 6. Then the failure envelope in the *H–V* plane is obtained and found to be similar to the experimental diagrams from Meyerhof (1953), Hansen (1970), Randolph and House (2002), Gourvenec and Randolph (2003), Cassidy *et al.* (2004), DNV (2013) and Ibsen *et al.* (2014) . Because of the high nonlinearity, the failure point forms an unsmooth curve.

It can be concluded that there is a strong interaction between vertical load and horizontal load. The diagram of vertical bearing capacity and horizontal bearing capacity approximates

a quarter-ellipse. As shown in Figures 8(a) and 8(b), the peak value is at $V = 0$. This agrees with Figures 7(b) on the *H–M* plane.

Combining the results in the *H–M* plane under different levels of vertical load (Figure 7) and the *H–V* plane (Figures 8(a) and 8(b)), the *H–M–V* 3D space envelope is plotted in Figures 9(a) and 9(b) based on simulations using MCC and HS respectively. The size of the inclined ellipse is controlled by vertical load.

4 Analytical formulas for the failure envelope

4.1 Analytical formula for the failure envelope based on HS model

According to the previous section, the failure envelope of the suction bucket foundation is like an inclined ellipse in the *H–M* plane. The failure surface of the suction bucket foundation can be reproduced by the formula introduced by Villalobos *et al.* (2009):

$$y = \left(\frac{H}{h_i V_0}\right)^2 + \left(\frac{M}{D m_i V_0}\right)^2 + 2e\frac{H}{h_i V_0}\frac{M}{D m_i V_0} - 1 = 0 \tag{1}$$

In this equation, the parameters h_i, m_i and e are used to determine the shape of the failure surface. The two variables h_i and m_i are used to describe, respectively, the intersection of the failure envelope and the axis of H/V_0 and M/DV_0. The eccentricity of the ellipse is expressed as e. The yield points obtained can be fitted by this formula.

Figure 10, shows how h_i and m_i changed with the value of V. It can be seen that the relation curves are similar to a quarter-circle and a quarter-ellipse, which is different from the proposed formulas. To obtain a more accurate result, the formulas of h_i and m_i are changed to the corresponding fitting formulas:

$$\frac{H}{H_0} + \left(\frac{V}{V_0}\right)^{3.6} = 1 \tag{2}$$

$$\frac{M/D}{M_0/D} + \left(\frac{V}{V_0}\right)^{2.5} = 1 \tag{3}$$

$$h_i = \frac{H_i}{V_0} = h_0\left(1-\left(\frac{V}{V_0}\right)^{3.6}\right) \tag{4}$$

$$m_i = \frac{M_i/D}{V_0} = m_0\left(1-\left(\frac{V}{V_0}\right)^{2.5}\right) \tag{5}$$

All the preceding equations describe the fitting equation in Figure 10(a), and for Figure 10(b), the fitting formulas are as follows:

$$h_i = \frac{H_i}{V_0} = h_0\left(1-\left(\frac{V}{V_0}\right)\right)\left(0.88\left(\frac{V}{V_0}\right)^2+1.08\left(\frac{V}{V_0}\right)+1\right) \tag{6}$$

$$m_i = \frac{M_i/D}{V_0} = m_0\left(1-\left(\frac{V}{V_0}\right)\right)\left(0.88\left(\frac{V}{V_0}\right)^2+1.08\left(\frac{V}{V_0}\right)+1\right) \tag{7}$$

The half of the inclined parabolic ellipsoid (failure surface in the *H*–*V*–*M* plane) can be obtained by the combination of Eqs. (1), (4) and (5):

$$\begin{aligned} F = &\left(1-\left(\frac{V}{V_0}\right)^{2.5}\right)^2\left(\frac{H}{h_0V_0}\right)^2+2e\left(1-\left(\frac{V}{V_0}\right)^{2.5}\right)\left(1-\left(\frac{V}{V_0}\right)^{3.6}\right)\frac{H}{h_0V_0}\frac{M}{Dm_0V_0} \\ &+\left(1-\left(\frac{V}{V_0}\right)^{3.6}\right)^2\left(\frac{M}{Dm_0V_0}\right)^2-\left(1-\left(\frac{V}{V_0}\right)^{2.5}\right)^2\left(1-\left(\frac{V}{V_0}\right)^{3.6}\right)^2=0 \end{aligned} \tag{8}$$

It also can be obtained by the combination of Eqs. (1), (6) and (7):

$$F = \left(\frac{H}{h_0V_0}\right)^2+\left(\frac{M}{Dm_0V_0}\right)^2+2e\frac{H}{h_0V_0}\frac{M}{Dm_0V_0}-F_V(V,V_0)=0 \tag{9}$$

and

$$F_V(V,V_0) = \left(1-\left(\frac{V}{V_0}\right)\right)\left(0.88\left(\frac{V}{V_0}\right)^2+1.08\left(\frac{V}{V_0}\right)+1\right) \tag{10}$$

The parameters obtained by fitting the numerical results with the optimal curve are shown in Table 4. According to Eqs. (8) and (9), the 3D failure surface for the suction bucket

foundation in clay are plotted in Figure 11. The correlation coefficient R^2 is estimated as 0.982 and 0.873, respectively, which indicates that Eq. (8) is more suitable for reproducing the 3D failure surface of the suction bucket foundation.

4.2 Alternative analytical formula for the failure envelope based on MCC model

Figure 12 shows how h_i and m_i changed with the value of V. It can be seen that the relation curves are similar to a quarter-circle and a quarter-ellipse, which is different from the proposed formulas. To obtain a more accurate result, the formulas of h_i and m_i are changed to the corresponding fitting formulas:

$$\left(\frac{H}{H_0}\right)^{\frac{25}{9}}+\left(\frac{V}{V_0}\right)^3=1 \tag{11}$$

$$\left(\frac{M/D}{M_0/D}\right)^{\frac{10}{9}}+\left(\frac{V}{V_0}\right)^3=1 \tag{12}$$

$$h_i=\frac{H_i}{V_0}=h_0\left(1-\left(\frac{V}{V_0}\right)^3\right)^{0.36} \tag{13}$$

$$m_i=\frac{M_i/D}{V_0}=m_0\left(1-\left(\frac{V}{V_0}\right)^3\right)^{0.9} \tag{14}$$

The half of the inclined parabolic ellipsoid (failure surface in the H–V–M plane) can be obtained by the combination of Eqs. (1), (13) and (14):

$$F=\left(1-\left(\frac{V}{V_0}\right)^3\right)^{1.08}\left(\frac{H}{h_0V_0}\right)^2+2e\left(1-\left(\frac{V}{V_0}\right)^3\right)^{0.54}\frac{H}{h_0V_0}\frac{M}{Dm_0V_0}+\left(\frac{M}{Dm_0V_0}\right)^2 -\left(1-\left(\frac{V}{V_0}\right)^3\right)^{1.8}=0 \tag{15}$$

The parameters obtained by fitting the numerical results with the optimal curve are shown in Table 4. According to Eq. (15), the 3D failure surface for the suction bucket foundation in clay are plotted in Figure 13. The correlation coefficient R^2 is estimated as

0.979, which indicates that Eq. (15) is suitable for reproducing the 3D failure surface of the suction bucket foundation.

4.3 Effect of L/D ratio

The failure of caisson foundation for different L/D ratio should be different, for which an additional case of L = 7.5 m and D = 3.75 m (L/D=2) was simulated only using HS model. Through radial displacement tests simulations, failure envelop in H-M plane at (a) χ=0, (b) different vertical load levels (Fig. 14), in H-V plane (Fig. 15), and the three-dimensional failure surface in H-M-V space (Fig. 16) were obtained. It can be found the L/D ratio significantly affects the size and the inclination of the failure envelop.

To examine the applicability of the failure surface formulation, the three-dimensional failure surface was fitted using the equation (9). As shown in Figure 16, good agreement was achieved which demonstrates that the failure surface formulation is applicable for different L/D ratios. Thus, the macro-element model based on above failure surface formulation should also be applicable for caisson foundations with different L/D ratios.

5 Hypoplastic macro-element modelling

5.1 General framework

Li *et al.* (2016) introduced the hypoplasticity macro-element for deep foundations, which can be seen as the starting point establishing use of a hypoplastic macro-element for foundations other than footings. Since then Jin *et al.* (2019) have developed the macro-element method for the caisson in sand under monotonic and cyclic loadings. The overall process is described hereafter, using the following conventions: tensors in bold letters, norm of a tensor written as ||·|| and the derivative of the variables with time represented by (·).

The generalised load vector $\boldsymbol{t}$ and displacement vector $\boldsymbol{u}$ are used to represent the mechanical response of suction bucket foundation,

$$\boldsymbol{t} := \{V, H, M/D\}^T \tag{16}$$

$$\boldsymbol{u} := \{w, u, D\theta\}^T \tag{17}$$

where V, H and M/D are the vertical, horizontal and generalised rotational force applied to the suction bucket and w, u and $D\theta$ are the vertical, horizontal and rotational displacements, respectively. D is the diameter of the bucket foundation for homogenising the dimensions of the $\boldsymbol{t}$ and $\boldsymbol{u}$ components. The vector $\boldsymbol{d}$ is defined as generalised velocity, which can be expressed as

$$\boldsymbol{d} := \dot{\boldsymbol{u}} \tag{18}$$

The macro-element formulas of hypoplasticity under monotonic loading conditions are expressed as

$$\dot{\boldsymbol{t}} = \mathcal{K}(\boldsymbol{t}, \boldsymbol{q}, \boldsymbol{d}) \tag{19a}$$

$$\mathcal{K} = \mathcal{L}(\boldsymbol{t}, \boldsymbol{q}) + \boldsymbol{N}(\boldsymbol{t}, \boldsymbol{q})\boldsymbol{\eta}^T \tag{19b}$$

$$\boldsymbol{\eta} = \frac{\boldsymbol{d}}{\|\boldsymbol{d}\|} \tag{19c}$$

where $\boldsymbol{q}$ is the internal variable pseudo-vector that accounts for the impacts of the previous loading history.

The difference between tangent stiffness $\mathcal{K}(\boldsymbol{t}, \boldsymbol{q}, \boldsymbol{d})$ and classical elastic–plastic tangent stiffness is that $\mathcal{K}$ is changing the generalised velocity direction $\boldsymbol{\eta}$, a property that is incremental and nonlinear. Moreover, $\mathcal{K}(\boldsymbol{t}, \boldsymbol{q}, \boldsymbol{d})$ has both a "linear" term ($\boldsymbol{L}$) and a "nonlinear" term ($\boldsymbol{N}$). $\mathcal{L}$ describes the initial linear constitutive relationship of the macro-element and also represents the stiffness at a load reversal point. As the stress state changes, $\boldsymbol{N}$ will modify the "linear" behaviour continuously.

To investigate the cyclic loadings, a definition of the "internal displacement" $\boldsymbol{\delta}$ proposed by Niemunis and Herle (1997) and Salciarini and Tamagnini (2009) is adopted. The formulations of the macro-element are thus modified as follows:

$$\dot{\boldsymbol{t}} = \mathcal{K}(\boldsymbol{t}, \boldsymbol{q}, \boldsymbol{\delta})\boldsymbol{d} \tag{20}$$

$$\mathcal{K} = \left[\rho^{\chi} m_T + (1 - \rho^{\chi}) m_R \right] \mathcal{L} + \begin{cases} \rho^{\chi}(1 - m_T)(\mathcal{L}\boldsymbol{\eta}_{\delta})\boldsymbol{\eta}_{\delta}^T + \rho^{\chi}\boldsymbol{N}\,\boldsymbol{\eta}_{\delta}^T & (\boldsymbol{\eta}_{\delta} \cdot \boldsymbol{\eta} > 0) \\ \rho^{\chi}(m_R - m_T)(\mathcal{L}\boldsymbol{\eta}_{\delta})\boldsymbol{\eta}_{\delta}^T & (\boldsymbol{\eta}_{\delta} \cdot \boldsymbol{\eta} \le 0) \end{cases} \tag{21}$$

The derivative of $\boldsymbol{\delta}$ (internal displacement) is expressed as:

$$\dot{\boldsymbol{\delta}} = \begin{cases} (\mathcal{I} - \rho^{\beta_r} \boldsymbol{\eta}_\delta \boldsymbol{\eta}_\delta^T)\boldsymbol{d} & (\boldsymbol{\eta}_\delta \cdot \boldsymbol{\eta} > 0) \\ \boldsymbol{d} & (\boldsymbol{\eta}_\delta \cdot \boldsymbol{\eta} \le 0) \end{cases} \tag{22}$$

The value of scalar ρ is [0,1], which can be obtained by the norm of $\boldsymbol{\delta}$, $\rho = \left(\frac{\|\boldsymbol{\delta}\|}{R} \right)$. m_T, m_R, χ, β_r and R are five constants; $\mathcal{I}$ is the identity matrix; and

$$\boldsymbol{\eta}_\delta = \begin{cases} \boldsymbol{\delta} / \|\boldsymbol{\delta}\| & (\delta \neq 0) \\ 0 & (\delta = 0) \end{cases} \tag{23}$$

It can be seen that to reproduce cyclic loadings of the suction bucket foundation, the "linear" and "nonlinear" constitutive relationships of the macro-element are modified by comparing Eqs. (19), (20) and (21). The matrix $\boldsymbol{L}$ is expressed as

$$\mathcal{L} = \frac{1}{m_R} \mathcal{K}^e \tag{24}$$

$$\mathcal{K}^e := \begin{bmatrix} k_{vv} & 0 & 0 \\ 0 & k_{hh} & k_{hm} \\ 0 & k_{hm} & k_{mm} \end{bmatrix} \tag{25}$$

where $\mathcal{K}^e$ is the elastic stiffness matrix and k represents the different dimensional stiffness of the bucket and soil system, which was similar to that of pile foundations (Li *et al.* 2016; Li *et al.* 2018). Because of the skirt of the suction bucket foundation, k_{hm} must be taken into account.

$\boldsymbol{N}$ is defined as

$$\boldsymbol{N}(\boldsymbol{t}) = -Y(\boldsymbol{t}) \mathcal{L} \boldsymbol{m}(\boldsymbol{t}) \tag{26}$$

$Y(\boldsymbol{t})$ is a scalar function that controls the nonlinearity degree, and $\boldsymbol{m}(\boldsymbol{t})$ is the unit gradient describing the direction of plastic flow. To define $\boldsymbol{Y}$ and $\boldsymbol{m}$ in Eq. (26), the ultimate failure surface $F(\boldsymbol{t})$ and the loading surface $f(\mathbf{t})$ are needed to be adopted.

5.2 Novel macro-element models

In this section, in seeking to establish $F(\boldsymbol{t})$ for a suction bucket foundation in clay, we use numerical calculation and simulation to find the 3D failure surface. We now review the details of the research discussed in previous sections. Different loading paths were selected to study the shape and size of the failure surface in the *H–M* plane, and as Figure 5 shows, a constant radial loading ratio was determined and the large displacements applied on the LRP of the suction bucket foundation to reach the ultimate strength under a constant vertical load. The end points of the loading paths are defined as the failure loci points (see Figure 6).

Villalobos *et al.* (2009) introduced a mathematical equation for reproducing the failure envelope in the *H*:*M/D* plane (Eq. (1)). In this equation, the parameters h_i, m_i and e are used to determine the shape of the failure surface. The two variables h_i and m_i are used to describe the intersection of the failure envelope and the axis of H/V_0 and M/DV_0, respectively. The eccentricity of the ellipse is expressed as e. Using least-squares regression, the yield points obtained in previous sections can be fitted by Eq. (1) (Villalobos et al., 2009), shown in Figure 17.

Figure 10(a) and Figure 12 show how h_i and m_i changed with the value of V/V_0. It can be seen the relation curves are similar with a quarter-circle and a quarter-ellipse. Eqs. (2) and (3) provide the fitting functions of HS model. Eqs. (11) and (12) provide the fitting functions of MCC model. The fitting equations of HS model are shown in Eqs. (2), (3), (4) and (5). Also, fitting equations of MCC model are shown in Eqs. (11), (12), (13) and (14).

V_0 has been determined by applying the K1-1 test; h_0 and m_0 are defined as the maximum h_i and m_i respectively, found at $V/V_0 = 0$. Note that Eqs. (4), (5), (13) and (14) can be adopted at the different levels of V. All the parameters of macro-element are shown in Table 5. Half of the inclined parabolic ellipsoid of HS model (failure envelop in the *H–V–M* plane; see Figure 11(a)) is expressed in Eq. (8). The failure surface in the *H–V–M* plane of MCC model (Figure 13) is expressed in Eq. (15).

As for the hypoplasticity framework, $F(\boldsymbol{t})$ is the boundary of the stress state for a suction bucket foundation in clay that functions as a bounding surface. Plasticity will develop, with the bounding surface reaching the full plastic state when the stress state of the foundation reaches the boundary surface. In this case, the current stress state can be considered to be lying on a smaller bounding surface, which is defined as loading surface, $f(\boldsymbol{t})$; see Figure 18.

With the development of plasticity, the size of the loading surface could enlarge as isotropic as the bounding surface. $Y(\boldsymbol{t})$ is used to define the nonlinearity degree as

$$Y(t) = \xi^{\kappa} \tag{27}$$

the value of ξ is [0,1], and it measures the distance between $f(\boldsymbol{t})$ and $F(\boldsymbol{t})$. κ is a material constant which can control the loading function evolution.

Geometrically, as seen in Figure 18, the loading surface $f(\boldsymbol{t})$ has the same shape as $F(\boldsymbol{t})$, but smaller, so the associated formulas can be described as

$$\begin{aligned} f = &\left(1-\left(\frac{V}{\xi V_0}\right)^{2.5}\right)^2\left(\frac{H}{\xi h_0 V_0}\right)^2 + 2e\left(1-\left(\frac{V}{\xi V_0}\right)^{2.5}\right)\left(1-\left(\frac{V}{\xi V_0}\right)^{3.6}\right)\frac{H}{h_0\xi V_0}\frac{M}{Dm_0\xi V_0} \\ &+\left(1-\left(\frac{V}{\xi V_0}\right)^{3.6}\right)^2\left(\frac{M}{Dm_0\xi V_0}\right)^2 - \left(1-\left(\frac{V}{\xi V_0}\right)^{2.5}\right)^2\left(1-\left(\frac{V}{\xi V_0}\right)^{3.6}\right)^2 = 0 \ (\text{by HS}) \end{aligned} \tag{28}$$

or

$$\begin{aligned} f = &\left(1-\left(\frac{V}{\xi V_0}\right)^{3}\right)^{1.08}\left(\frac{H}{\xi h_0 V_0}\right)^2 + 2e\left(1-\left(\frac{V}{\xi V_0}\right)^{3}\right)^{0.54}\frac{H}{\xi h_0 V_0}\frac{M}{D\xi m_0 V_0} + \left(\frac{M}{D\xi m_0 V_0}\right)^2 \\ &-\left(1-\left(\frac{V}{\xi V_0}\right)^{3}\right)^{1.8} = 0 \ (\text{by MCC}) \end{aligned} \tag{29}$$

By plugging the current stress state (H, M/D, V) into Eqs. (28) or (29), we can obtain the root value of $\xi \in [0,1]$ in this nonlinear function. It can be calculated numerically by bisection or Newton-Raphson method.

$\boldsymbol{m}(\boldsymbol{t})$ is the direction of normalised plastic flow, taken as the normalised gradient of the $f(\boldsymbol{t})$ at the current stress state (Figure 18). According to the associative plastic flow rule, $\boldsymbol{m}(\boldsymbol{t})$ is given by

$$\boldsymbol{m}(\boldsymbol{t}) = \frac{\partial f / \partial \boldsymbol{t}}{\left\| \partial f / \partial \boldsymbol{t} \right\|} \tag{30}$$

5.3 Parameters of macro-element models and calibration

The macro-element parameters have been divided into four groups, as shown in Table 5:

four parameters that determine the failure surface, four pseudo-elastic stiffness coefficients, a hardening parameter used to control macro-element stiffness decay under monotonic loadings and five parameters that control the behaviour of the foundation under cyclic loadings.

The hypoplastic macro-elements for suction bucket foundations in clay are implemented in MATLAB. Experimental results are used to identify and validate these parameters. Using appropriate loading conditions and numerical simulation, the pseudo-elastic stiffness coefficients of macro-elements can be determined, as shown in Figure 19 (Li *et al.* 2016). For instance, when the rotation remains unchanged, a small horizontal displacement applied at LRP can obtain the value of k_{mh}. The results are shown in Table 5.

The K1-2 test was selected to calibrate the value of κ. Extra macro-element simulations in the H:u plane for other values of κ under the same loading condition are shown in Figure 20. Based on comparisons with experimental data, κ = 0.9 was chosen for the constant of the function of HS model, and κ = 0.6 was chosen for MCC model.

Since there are no cyclic tests available in Watson (2000), the field test at Bothkennar and laboratory test under cyclic loadings by Kelly *et al.* (2006) were adopted to evaluate the predictive ability of the proposed macro-elements. Since there are no tests under monotonic loading available, we just adopted the parameters of the case of Kaolin clay foundation as the cyclic loading states are inside of the yield envelope. The parameters for cyclic behaviour have been calibrated by trial and error comparing the simulated and experimental/in-situ results of Kelly *et al.* (2006). More specifically, the constants β^{r} and χ are less sensitive. The size of the pseudo-elastic region R can be inferred from the length of the pseudo-linear part of the load-displacement curve during unloading or reloading, while the parameters m_{R} and m_{T} affect the stiffness ratio of the system under reverse or tangential loading and continuous loading conditions. The calibrated values of the 5 parameters are summarized in Table 5.

The results of cyclic moment under small deformation moment loading ($M/[s_u(2R)^3]$ = 0.25) from the field test at Bothkennar and laboratory test are shown in Figures 21(a) and 21(b) which are used for parameters calibration. The simulated results in Figures 21(c) and 21(d) well agree with the observed response of the system in the moment cyclic loading tests, indicating a good descriptive performance of the macro-element models.

Note that all parameters can also be identified through the inverse analysis using optimisation or Bayesian methods, as shown by Yin *et al*. (2016, 2017, 2018) and Jin *et al*.

(2016, 2017, 2018, 2019a, 2019b) for advanced constitutive models of clay or sand.

5.4 Validation of models

The swipe test K1-3 was adopted to validate the predicative performance of the macro-element models that adopted the parameters of Table 5. Figure 22 shows that the calculation results are basically consistent by comparing results of the experiment and the macro-elements under monotonic loading.

The results of cyclic moment under large deformation moment loading ($M/[s_u(2R)^3] = 0.312$) from the field test at Bothkennar and laboratory test are shown in Figures 23(a) and 23(b) for predictions. The comparison between experimental results and simulated results, shown in Figure 23(c) and 23(d), demonstrates that both macro-elements based on HS and MCC well describe the observed response of the system in the moment cyclic loading tests, indicating a good predictive ability of the macro-element models. Both macro-elements are applicable and the one based on HS has slightly better performance than that of MCC. Furthermore, by comparing the macro-element results simulated by adopting HS and MCC models, it can be found that, even though the constitutive models and three-dimensional failure surface selected are a little bit different, the results are close at last.

In conclusion, the behaviours of the complex loading pattern on the horizontal and rotational dimension are well regenerated by the macro-elements. The excellent comparison between the macro-element predictions and the observed response in validation tests indicates that the proposed approach is capable of reproducing the foundation-soil system behaviour with the same level of accuracy of advanced non-linear three-dimensional finite element simulations, but with a dramatic reduction of the computational cost. Moreover, the macro-elements are robust without any convergence problem usually happened in finite element calculations.

5.5 Model validation by other tests

In order to further evaluate the predictive ability of the proposed macro-elements, a series of swipe tests of caisson foundation with L = 3 m and D = 6 m in Kaolin clay conducted by Cassidy et al. (2004) was adopted. Note that only the macro-element model based on HS is used since the one based on MCC has similar predictive ability shown in

previous sections. Four swipe tests were carried out by applying horizontal displacement under constant vertical forces without rotation and moment. Four different vertical forces bigger than the vertical bearing capacity (V_0 = 0.992 MN) were applied for four swipe tests: (Swipe-1) V_0 = 1.268 MN, (Swipe-2) V_0 = 1.601 MN, (Swipe-3) V_0 = 1.919 MN and (Swipe-4) V_0 = 2.352 MN.

For macro-element parameters, h_0 = 0.288 and m_0 = 0.073 were measured based on failure envelop of caisson foundations provided by Cassidy et al. (2004). Then, other parameters from the previous case (Table 5) were directly adopted since two cases of caisson foundation are quit similar. The κ was found sensitive and thus re-calibrated by using the swipe-2. As shown in Figure 24 based on comparisons with experimental data, κ = 0.62 was determined. The remaining three swipe tests were adopted hereafter to evaluate the predictive ability of the macro-element. Figure 25 shows the comparison between the model test results and the macro-element predictions. A fairly good agreement is observed for all the swipe tests.

6 Conclusion

Through finite element analysis and development of new macro-element models, the mechanical response of a suction bucket foundation in clay was numerically investigated in this study. The main conclusions and contributions are concluded as follows:

(1) Using PLAXIS-3D, the MCC and HS models were adopted to simulate the mechanical response of a suction bucket foundation in clay subjected to complex loading combinations. Based on a comparison of numerical results with experimental ones, both MCC and HS models were validated and selected to study the 3D bearing capacity thenceforth. Then, new analytical formulations for expressing the 3D failure envelope in the *V–H–M* space were proposed based on the results of numerical simulations.

(2) Two novel macro-element models based on MCC and HS respectively were proposed to reproduce the mechanical response of a suction bucket foundation in clay under the same framework of hypoplasticity. It is shown that the macro-elements are able to reproduce the nonlinear behaviour of the suction bucket foundation in clay under the monotonic and cyclic loadings by comparing the predicted results with experimental ones. The computational cost and robustness when using the macro-element is much lower and

stronger than those for classical finite element analysis of the same problem, making the macro-element model valuable for foundation design in the field of marine engineering.

Acknowledgments

This research was financially supported by the Research Grants Council (RGC) of Hong Kong Special Administrative Region Government (HKSARG) of China (Grant No.: PolyU R5037-18F) and the Key Special Project for Introduced Talents Team of Southern Marine Science and Engineering Guangdong Laboratory (Guangzhou) (No.: GML2019ZD0503).

References

Allersma, H., Kirstein, A., Brinkgreve, R., Simon, T., 1999. Centrifuge and numerical modelling of horizontally loaded suction piles, The Ninth International Offshore and Polar Engineering Conference. International Society of Offshore and Polar Engineers 10 (3): 223-235.

Barari, A., Ibsen, L.B., 2011. Effect of embedment on the vertical bearing capacity of bucket foundations in clay, Proc. of 2011 Pan-Am CGS Geotechnical Conf., Toronto, Canada

Barari, A., Ibsen, L.B., 2012. Undrained response of bucket foundations to moment loading. Applied ocean research 36, 12-21.

Cao, J., 2003. Centrifuge modeling and numerical analysis of the behaviour of suction caissons in clay (Doctoral dissertation, Memorial University of Newfoundland).

Cao, J., Audibert, J., Al-Khafaji, Z., Phillips, R., Popescu, R., 2004. Excess pore pressures induced by installation of suction caissons in NC clays. Underwater Technology 26 (1), 13-18.

Cassidy, M., Byrne, B., Randolph, M., 2004. A comparison of the combined load behaviour of spudcan and caisson foundations on soft normally consolidated clay. Géotechnique 54 (2), 91-106.

Cassidy, M., Randolph, M., Byrne, B., 2006. A plasticity model describing caisson behaviour in clay. Applied ocean research 28 (5), 345-358.

Cheng, X., Wang, J., Wang, Z., 2016. Incremental elastoplastic FEM for simulating the deformation process of suction caissons subjected to cyclic loads in soft clays. Applied ocean research 59, 274-285

Clukey, E., Morrison, M., Gamier, J., Corté, J., 1995. The response of suction caissons in normally consolidated clays to cyclic TLP loading conditions, Proc. Annual Offshore Technology Conf., Houston, Paper OTC 7796.

di Prisco, C.G., Massimino, M.R., Maugeri, M., Nicolosi, M., Nova, R., 2006. Cyclic numerical analyses of Noto Cathedral: soil-structure interaction modelling. Rivista Italiana di Geotecnica 48, 49-64.

di Prisco, C.G., Nova, R., Perotti, F., Sibilia, A., 2003a. Shallow footings under cyclic loading: experimental behaviour and constitutive modelling. In Geotechnical analysis of the Seismic Vulnerability of Historical Monuments. Maugei M, Nova R, Eds. Pàton, 2003: 99-121.

di Prisco, C.G., Nova, R., Sibilia, A., 2003b. Analysis of soil-foundation interaction of tower structures under cyclic loading. In Geotechnical analysis of the Seismic Vulnerability

of Historical Monuments. Maugeri, M., Nova, R., Eds. Pàtron: 123-136.

DNV, D.N.V. 2013. Design of offshore wind turbine structures. Standard DNV-OSJ101, Det Norske Veritas AS (DNV).

Foglia, A., Gottardi, G., Govoni, L., Ibsen, L.B., 2015. Modelling the drained response of bucket foundations for offshore wind turbines under general monotonic and cyclic loading. Applied ocean research 52, 80-91.

Fuglsang, L., Steensen-Bach, J., 1991. Breakout resistance of suction piles in clay, Proceedings of the international conference: centrifuge, 153-159.

Gerolymos, N., Zafeirakos, A., Karapiperis, K., 2015. Generalized failure envelope for caisson foundations in cohesive soil: static and dynamic loading. Soil Dynamics and Earthquake Engineering 78, 154-174.

Gottardi, G., Houlsby, G., Butterfield, R., 1999. Plastic response of circular footings on sand under general planar loading. Géotechnique 49 (4), 453-470.

Gourvenec, S., Randolph, M., 2003. Effect of strength non-homogeneity on the shape of failure envelopes for combined loading of strip and circular foundations on clay. Géotechnique 53 (6), 575-586.

Guo, Z., Wang, L., Yuan, F., Li, L., 2012. Model tests on installation techniques of suction caissons in a soft clay seabed. Applied ocean research 34, 116-125.

Hansen, J.B., 1970. A revised and extended formula for bearing capacity. Copenhagen: Danish Geotechnical Institute 28: 5-11.

Harireche, O., Mehravar, M., Alani, A.M., 2013. Suction caisson installation in sand with isotropic permeability varying with depth. Applied ocean research 43, 256-263.

Houlsby, G., Kelly, R., Huxtable, J., Byrne, B., 2005. Field trials of suction caissons in clay for offshore wind turbine foundations. Géotechnique 55: 287-296.

Ibsen, L.B., Larsen, K.a., Barari, a., 2014. Calibration of Failure Criteria for Bucket Foundations on Drained Sand under General Loading. Journal of geotechnical and geoenvironmental engineering 140, 04014033.

Jin, Y.F., Wu, Z.-X., Yin, Z.-Y., Shen, J.S., 2017. Estimation of critical state-related formula in advanced constitutive modeling of granular material. Acta Geotechnica 12 (6), 1329-1351.

Jin, Y.F., Yin, Z.-Y., Wu, Z.-X., Daouadji, A., 2018. Numerical modeling of pile penetration in silica sands considering the effect of grain breakage. Finite Elements in Analysis and Design 144, 15-29.

Jin, Y.F., Yin, Z.-Y., Zhou, W.-H., Horpibulsuk, S., 2019. Identifying parameters of

advanced soil models using an enhanced transitional Markov chain Monte Carlo method. Acta Geotechnica, 1-23.

Jin, Y.F., Yin, Z.-Y., Zhou, W.-H., Shao, J.-F., 2019. Bayesian model selection for sand with generalization ability evaluation. International Journal for Numerical and Analytical Methods in Geomechanics, 2019, 43.14: 2305-2327.

Jin, Y.F., Yin, Z.-Y., Shen, S.L., Hicher, P.Y., 2016. Selection of sand models and identification of parameters using an enhanced genetic algorithm. International Journal for Numerical and Analytical Methods in Geomechanics 40 (8), 1219-1240.

Jin, Z., Yin, Z.-Y., Kotronis, P., Li, Z., Tamagnini, C., 2019. A hypoplastic macroelement model for a caisson foundation in sand under monotonic and cyclic loadings. Marine Structures 66, 16-26.

Kelly, R., Houlsby, G., Byrne, B., 2006. A comparison of field and laboratory tests of caisson foundations in sand and clay. Géotechnique **56**(9):617-626.

Kim, D.-J., Choo, Y.W., Kim, J.-H., Kim, S., Kim, D.-S., 2014. Investigation of monotonic and cyclic behavior of tripod suction bucket foundations for offshore wind towers using centrifuge modeling. Journal of Geotechnical and Geoenvironmental Engineering 140 (5), 04014008.

Kim, Y., Kim, K., Cho, Y., Bang, S., Jones, K., 2005. Centrifuge model tests on embedded suction anchors. The Fifteenth International Offshore and Polar Engineering Conference, International Society of Offshore and Polar Engineers, Seoul, Korea: 431-435.

Kourkoulis, R., Lekkakis, P., Gelagoti, F., Kaynia, A., 2014. Suction caisson foundations for offshore wind turbines subjected to wave and earthquake loading: effect of soil-foundation interface. Géotechnique 64 (3), 171.

Li, Z., Kotronis, P., Escoffier, S., Tamagnini, C., 2016. A hypoplastic macroelement for single vertical piles in sand subject to three-dimensional loading conditions. Acta Geotechnica 11 (2), 373-390.

Li, Z., Kotronis, P., Escoffier, S., Tamagnini, C., 2018. A hypoplastic macroelement formulation for single batter piles in sand. International Journal for Numerical and Analytical Methods in Geomechanics 42 (12), 1346-1365.

Lu, X., Wu, Y., Jiao, B., Wang, S., 2007. Centrifugal experimental study of suction bucket foundations under dynamic loading. Acta Mechanica Sinica 23 (6), 689-698.

Meyerhof, G.t., 1953. The bearing capacity of foundations under eccentric and inclined loads. Proc. of the 3rd Int. Conf. on SMFE (1): 440-445.

Muduli, P.K., Das, M.R., Samui, P., Kumar Das, S., 2013. Uplift capacity of suction caisson

in clay using artificial intelligence techniques. Marine Georesources & Geotechnology 31 (4), 375-390.

Nguyen-Sy, L., Houlsby, G.T., 2005. The theoretical modelling of a suction caisson foundation using hyperplasticity theory. Frontiers in Offshore Geotechnics II, Perth, 417.

Niemunis, A., Herle, I., 1997. Hypoplastic model for cohesionless soils with elastic strain range. Mechanics of Cohesive‐frictional Materials: An International Journal on Experiments, Modelling and Computation of Materials and Structures 2 (4), 279-299.

Raines, R.D., Garnier, J., 2008. Physical modeling of suction piles in clay, ASME 2004 23rd International Conference on Offshore Mechanics and Arctic Engineering. American Society of Mechanical Engineers Digital Collection, 621-631.

Randolph, M., House, A., 2002. Analysis of suction caisson capacity in clay. Proc. Annual Offshore Technology Conf., Houston, Paper OTC 14236

Renzi, R., Maggioni, W., Smits, F., Manes, V., 1991. A centrifugal study on the behavior of suction piles, Proc. Int. Conf. on Centrifuge Modelling-Centrifuge, 169-176.

Salciarini, D., Tamagnini, C., 2009. A hypoplastic macroelement model for shallow foundations under monotonic and cyclic loads. Acta Geotechnica 4 (3), 163-176.

Samui, P., Das, S., Kim, D., 2011. Uplift capacity of suction caisson in clay using multivariate adaptive regression spline. Ocean Engineering 38 (17-18), 2123-2127.

Schanz, T., Vermeer, P., Bonnier, P., 1999. The hardening soil model: formulation and verification. Beyond 2000 in computational geotechnics, 281-296.

Skau, K.S., Grimstad, G., Page, A.M., Eiksund, G.R., Jostad, H.P., 2018. A macro-element for integrated time domain analyses representing bucket foundations for offshore wind turbines. Marine Structures 59, 158-178.

Tjelta, T.-l., 1994. Geotechnical aspects of bucket foundations replacing piles for the Europipe 16/11-E jacket. Offshore Technology Conference, Houston, paper OTC 7379.

Vásquez, L.G., Maniar, D.R., Tassoulas, J.L., 2010. Installation and axial pullout of suction caissons: numerical modeling. Journal of Geotechnical and Geoenvironmental Engineering 136 (8), 1137-1147.

Villalobos, F.A., Byrne, B.W., Houlsby, G.T., 2009. An experimental study of the drained capacity of suction caisson foundations under monotonic loading for offshore applications. Soils and foundations 49 (3), 477-488.

Villalobos, F.A., Byrne, B.W., Houlsby, G.T., 2010. Model testing of suction caissons in clay subjected to vertical loading. Applied ocean research 32 (4), 414-424.

Watson, P.G. 1999. Performance of Skirted Foundations for Offshore Structures. PhD Thesis, The University of Western Australia.

Watson, P., Randolph, M., 1997. Vertical capacity of caisson foundations in calcareous sediments, The Seventh International Offshore and Polar Engineering Conference, Hawaii, USA, 152-159.

Yin, Z.-Y., Jin, Y.F., Huang, H.-W., Shen, S.-L., 2016. Evolutionary polynomial regression based modelling of clay compressibility using an enhanced hybrid real-coded genetic algorithm. Engineering geology 210, 158-167.

Yin, Z.-Y., Jin, Y.F., Shen, S.-L., Huang, H.-W., 2017. An efficient optimization method for identifying parameters of soft structured clay by an enhanced genetic algorithm and elastic–viscoplastic model. Acta Geotechnica 12 (4), 849-867.

Yin, Z.-Y., Jin, Y.F., Shen, J.S., Hicher, P.Y., 2018. Optimization techniques for identifying soil parameters in geotechnical engineering: comparative study and enhancement. International Journal for Numerical and Analytical Methods in Geomechanics 42 (1), 70-94.

Zdravkovic, L., Potts, D., Jardine, R., 1998. Pull-out capacity of bucket foundations in soft clay. Proceedings of the international conference on offshore site investigation and foundation behaviour ± New Frontiers, Vol. SUT 1, 301-324.

Zdravković, L., Potts, D., Jardine, R., 2001. A parametric study of the pull-out capacity of bucket foundations in soft clay. Géotechnique 51 (1), 55-67.

Zhang, J., Yan, D., Sun, G., Li, W., Lu, X., 2003. Development of a dynamic loading device for suction pile in centrifuge, BGA International Conference on Foundations: Innovations, observations, design and practice: Proceedings of the international conference organised by British Geotechnical Association and held in Dundee, Scotland on 2–5th September 2003. Thomas Telford Publishing, 985-990.

Zhang, J., Zhang, L., Lu, X., 2007. Centrifuge modeling of suction bucket foundations for platforms under ice-sheet-induced cyclic lateral loadings. Ocean Engineering 34 (8-9), 1069-1079.

Zhang P, Chen RP, Wu HN, 2019. Real-time Analysis and Regulation of EPB Shield Steering Using Random Forest. Automation in Construction. 106: 101860.

Zhang P, Chen RP, Wu HN, Liu Yuan. 2020. Ground settlement induced by tunneling Crossing interface of water-bearing mixed ground: a lesson from Changsha, China. Tunnelling and Underground Space Technology, 96, 103224.

Zhang, P., Ding, H., Le, C., 2013. Installation and removal records of field trials for two mooring dolphin platforms with three suction caissons. Journal of waterway, port,

coastal, and ocean engineering 139 (6), 502-517.

Zhang, P., Guo, Y., Liu, Y., Ding, H., Le, C., 2015. Model tests on sinking technique of composite bucket foundations for offshore wind turbines in silty clay. Journal of Renewable and Sustainable Energy 7 (3), 033113.

Zhou, H., Randolph, M.F., 2006. Large deformation analysis of suction caisson installation in clay. Canadian Geotechnical Journal 43 (12), 1344-1357.

Tables

Table 1 Values of parameters and initial state variables of the MCC model for Kaolin clay

Parameter	Value
Poisson's ratio, v'	0.3
Compression index, λ	0.278
Swelling index, κ	0.030
Initial void ratio, e_0	1.27
Slope of the critical state line, M	0.83

Table 2 Translation and rotation boundary conditions for the bucket.

Direction	Translation condition	Rotation condition
x	Free	Fixed
y	Fixed	Free
z	Free	Fixed

Table 3 Adopted centrifugal tests of suction bucket foundation in Kaolin Clay

Test series	Description
K1-1	Undrained vertical bearing capacity
K1-2	Large displacement, Sideswipe test under $V=0$
K1-3	Large displacement, Sideswipe test under $V=V'$ (V'/A=32 kPa)

Table 4 Parameters of failure surface for the suction bucket foundation

Parameter	Name	Value (HS)	Value (MCC)
V_0	Vertical bearing capacity: kN	2150	1800
h_0	Dimension of failure surface (horizontal)	0.213	0.245
m_0	Dimension of failure surface (moment)	0.101	0.124
e	Eccentricity of failure surface	0.768	0.80

Table 5 Parameters of the macro-element models based on HS and MCC

Group	Parameters	Description	Value (HS)	Value (MCC)
Failure surface	V_0 (kN)	Vertical bearing capacity	2150	1800
	h_0 (-)	Dimension of failure surface (horizontal)	0.213	0.245
	m_0 (-)	Dimension of failure surface (moment)	0.101	0.124
	e (-)	Eccentricity of failure surface	0.768	0.8
Pseudo-elastic stiffness	k_{vv} (kN/m)	Vertical stiffness	4024	4024
	k_{hh} (kN/m)	Horizontal stiffness	2261	2261
	k_{mm} (kN/m)	Rotational stiffness	854.8	854.8
	k_{hm} , k_{mh} (kN/m)	Coupled translation-rotation stiffness	-835.0	-835.0
Hardening parameter	κ (-)	Loading function constant	0.9	0.6
Cyclic behaviour (intergranular strain)	m_R (-)	Stiffness at load reversal point	5	5
	m_T (-)	Stiffness when neutral loading	2	2
	χ (-)	Transition of stiffness	0.5	0.5
	β^r (-)	Rate of evolution of intergranular strain	0.5	0.5
	R (-)	Range of linearity	0.02	0.02

Figures

Figure 1

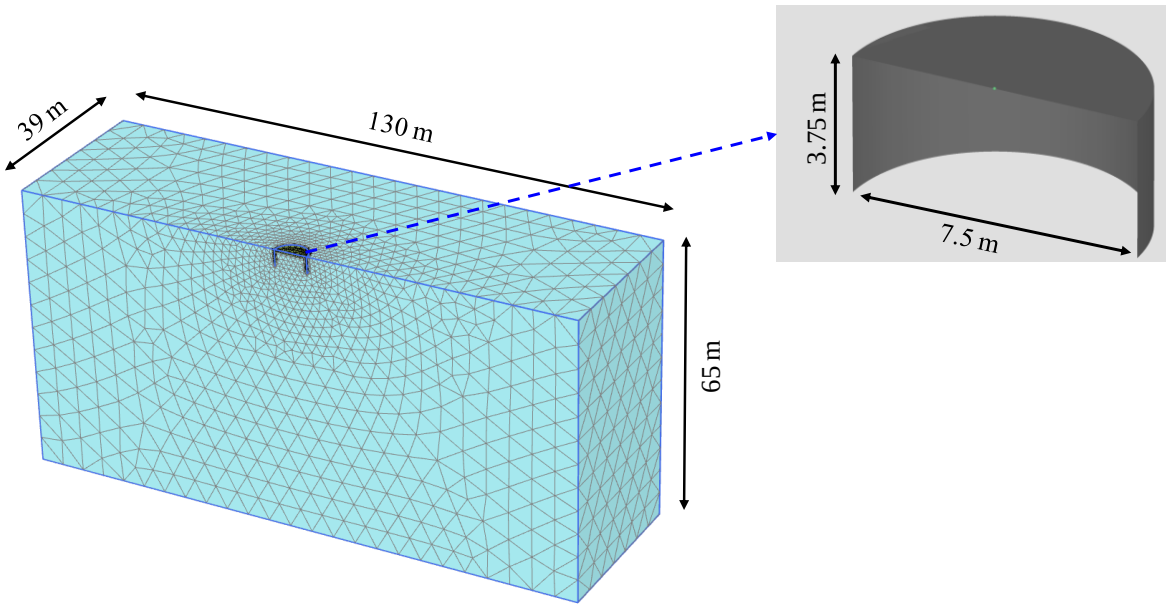

Figure 2

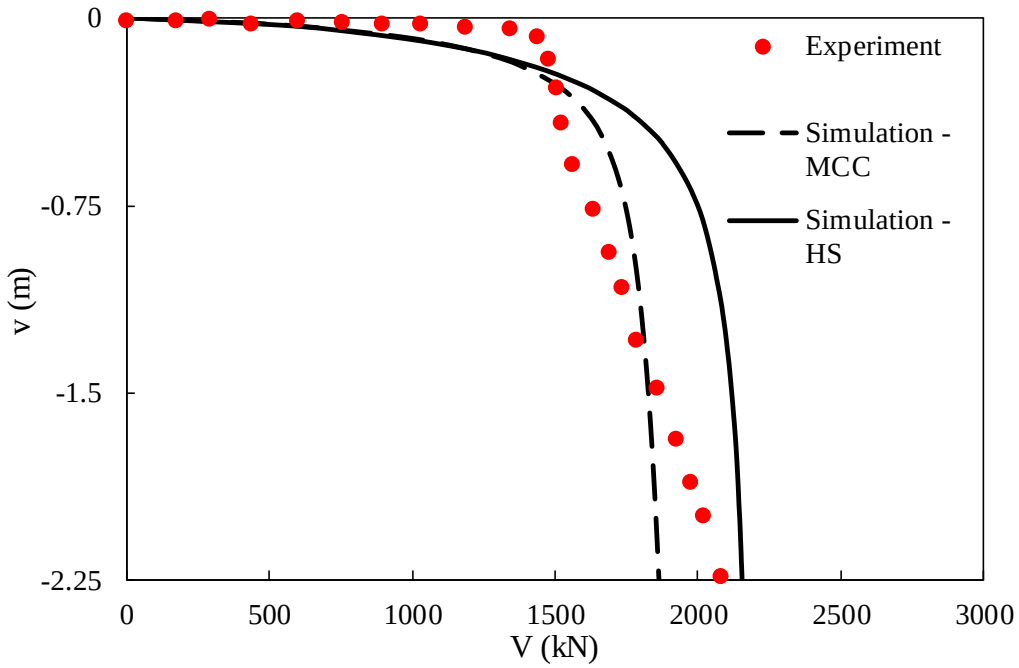

Figure 3

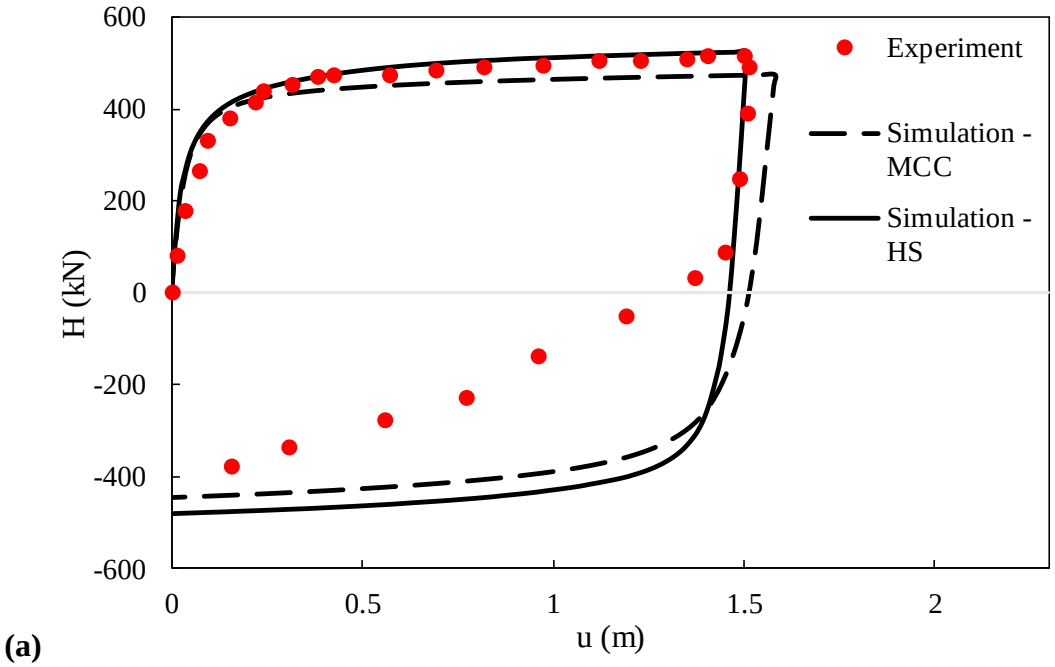
600
400
200
0
-200
-400
-600
H (kN)
0
0.5
1
1.5
2
u (m)
Experiment
Simulation - MCC
Simulation - HS

(a)

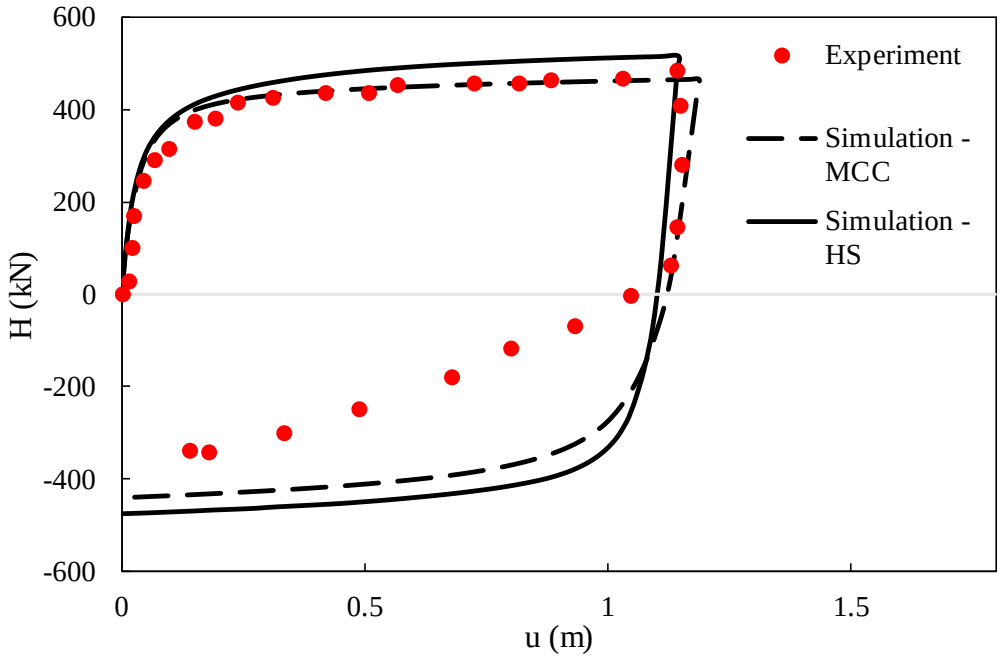
600
400
200
0
-200
-400
-600
H (kN)
0
0.5
1
1.5
u (m)
Experiment
Simulation - MCC
Simulation - HS

(b)

Figure 4

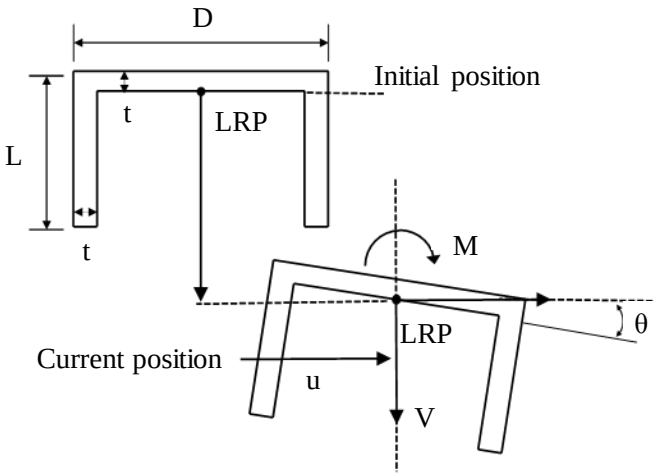

Figure 5

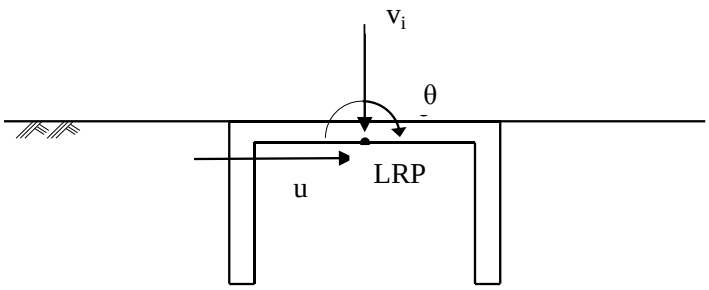

Figure 6

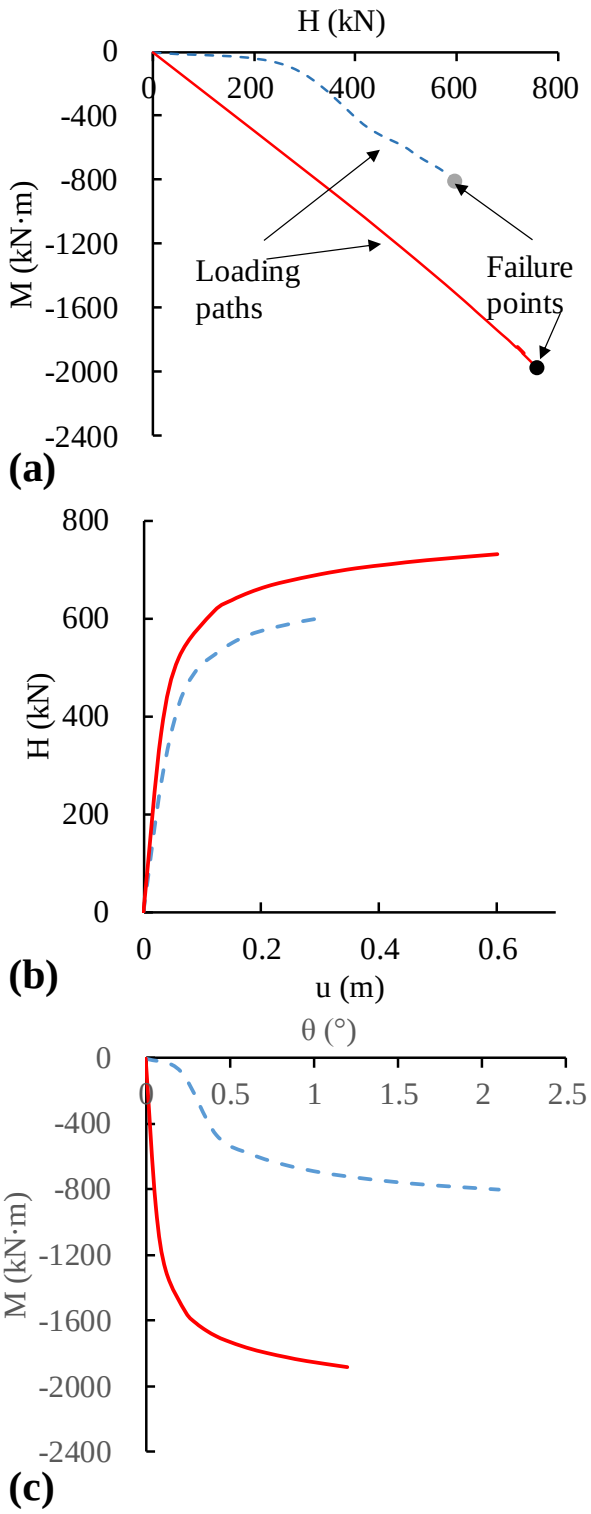
H (kN)
0
0
200
400
600
800
-400
-800
-1200
-1600
-2000
-2400
M (kN·m)
Loading paths
Failure points
(a)
800
600
400
200
0
H (kN)
0
0.2
0.4
0.6
u (m)
(b)
θ (°)
0
0
0.5
1
1.5
2
2.5
-400
-800
-1200
-1600
-2000
-2400
M (kN·m)
(c)

Figure 7

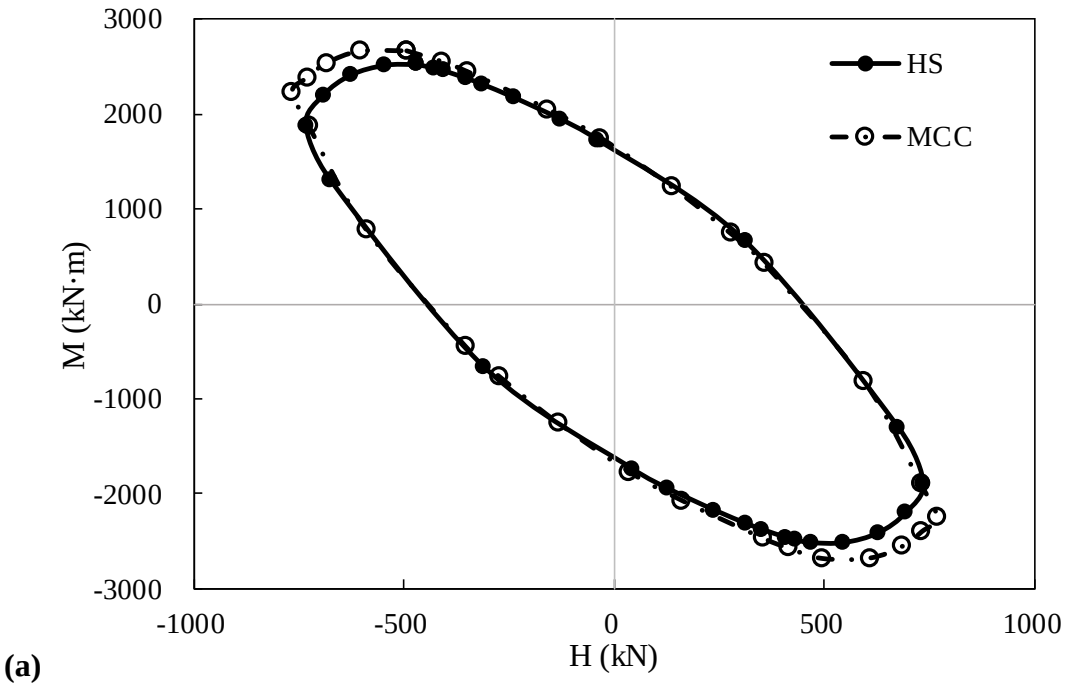
3000
2000
1000
0
-1000
-2000
-3000
M (kN·m)
-1000
-500
0
500
1000
H (kN)
HS
MCC

(a)

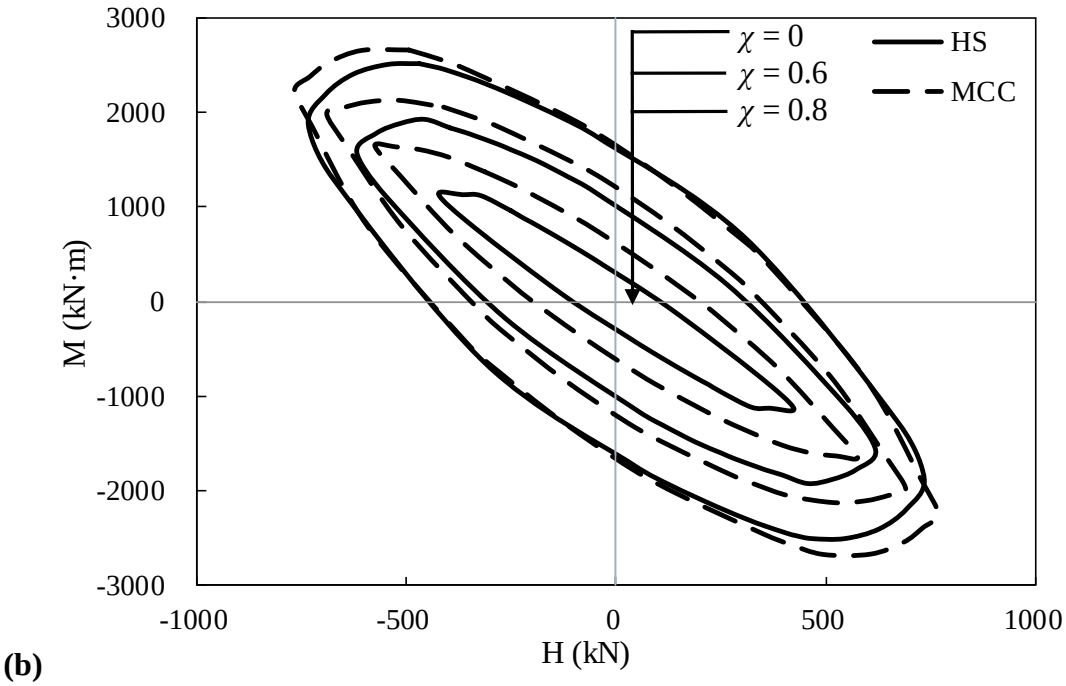
3000
2000
1000
0
-1000
-2000
-3000
M (kN·m)
-1000
-500
0
500
1000
H (kN)
χ = 0
χ = 0.6
χ = 0.8
HS
MCC

(b)

Figure 8

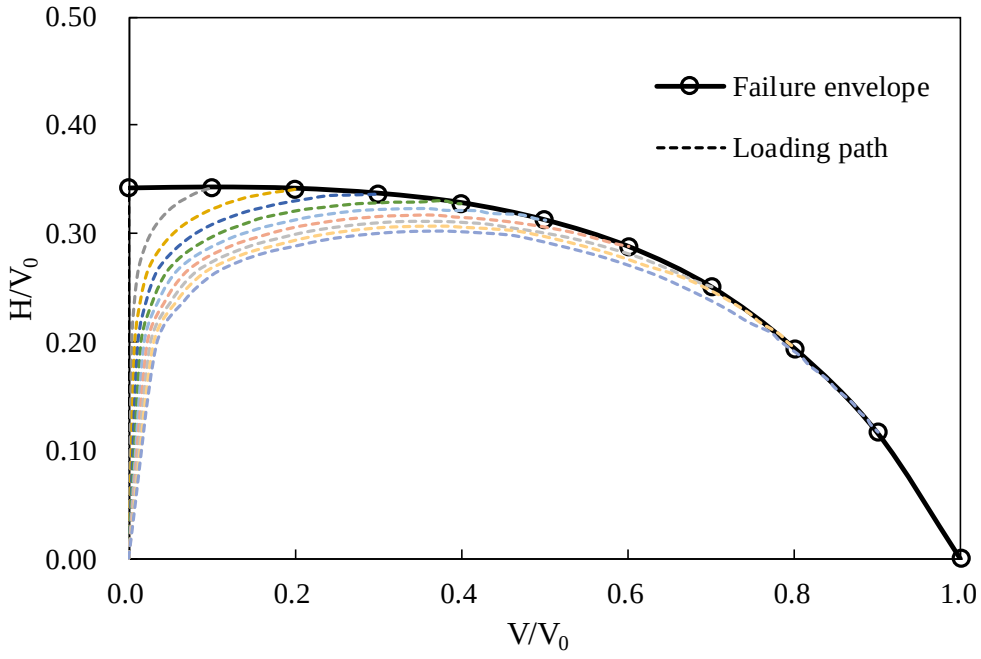
0.50
0.40
0.30
0.20
0.10
0.00
H/V0
0.0
0.2
0.4
0.6
0.8
1.0
V/V0
Failure envelope
Loading path

(a)

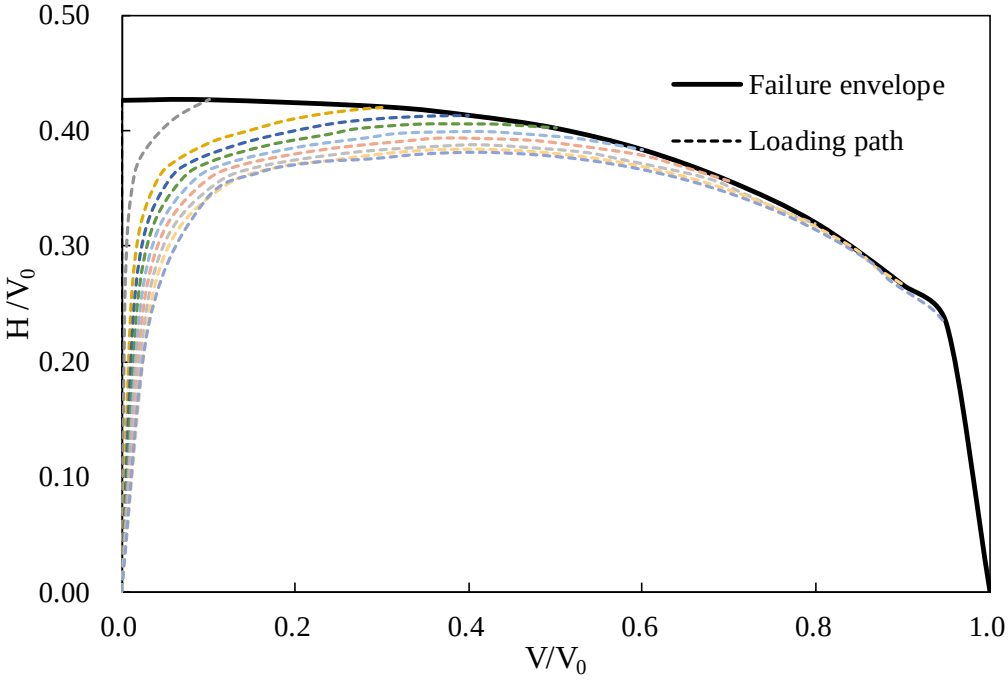
0.50
0.40
0.30
0.20
0.10
0.00
H /V0
0.0
0.2
0.4
0.6
0.8
1.0
V/V0
Failure envelope
Loading path

(b)

Figure 9

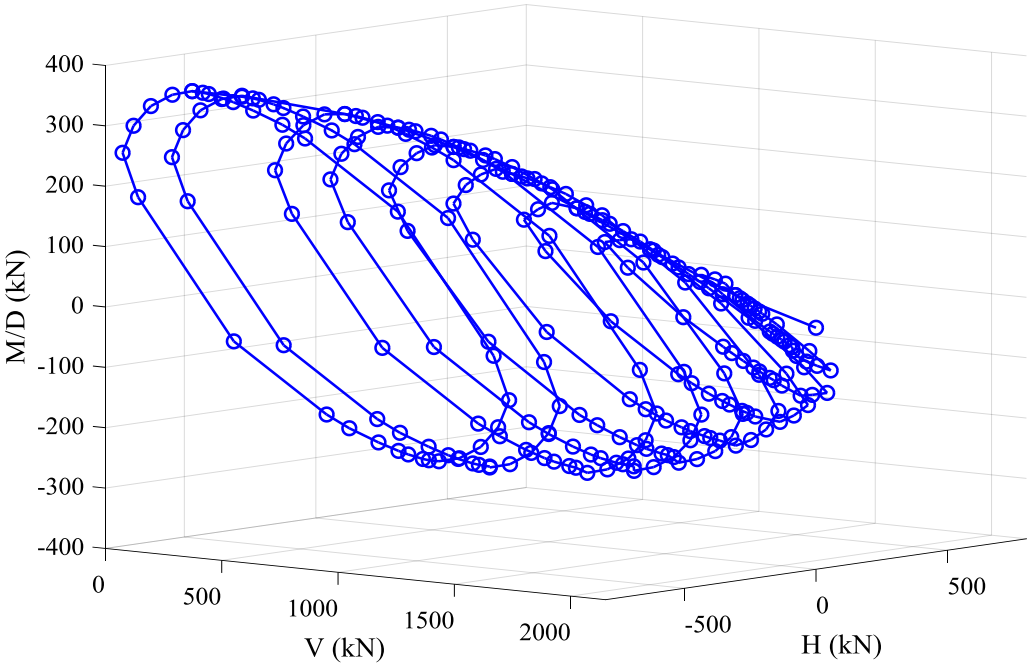
400
300
200
100
0
-100
-200
-300
-400
M/D (kN)
0
500
1000
1500
2000
V (kN)
-500
0
500
H (kN)

(a)

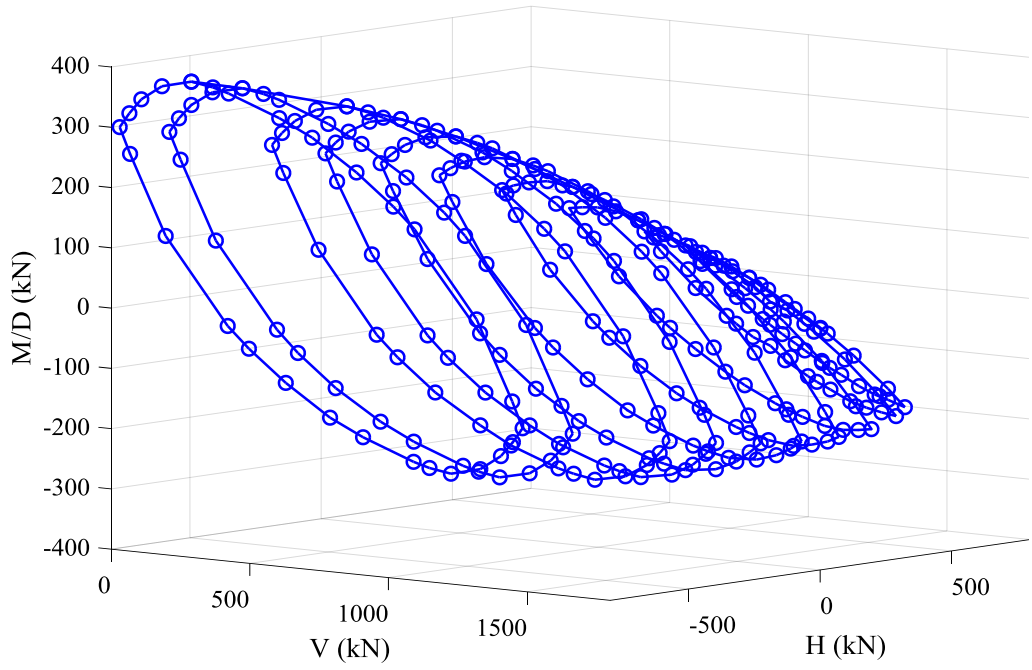
400
300
200
100
0
-100
-200
-300
-400
M/D (kN)
0
500
1000
1500
V (kN)
-500
0
500
H (kN)

(b)

Figure 10

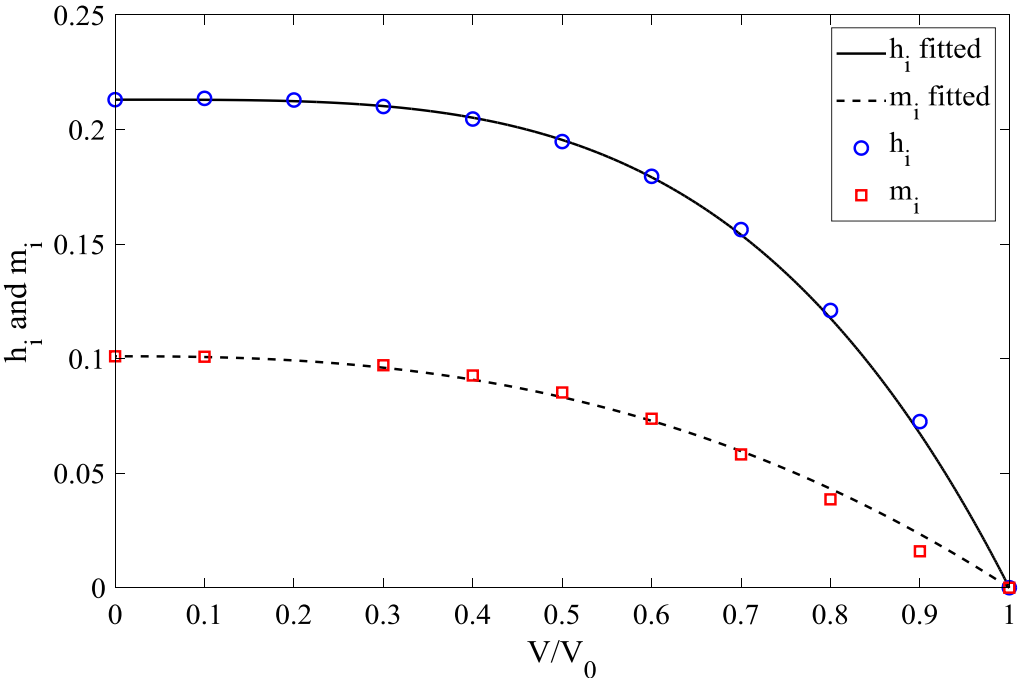
0.25
0.2
0.15
0.1
0.05
0
h_i and m_i
0
0.1
0.2
0.3
0.4
0.5
0.6
0.7
0.8
0.9
1
V/V_0
h_i fitted
m_i fitted
h_i
m_i

(a)

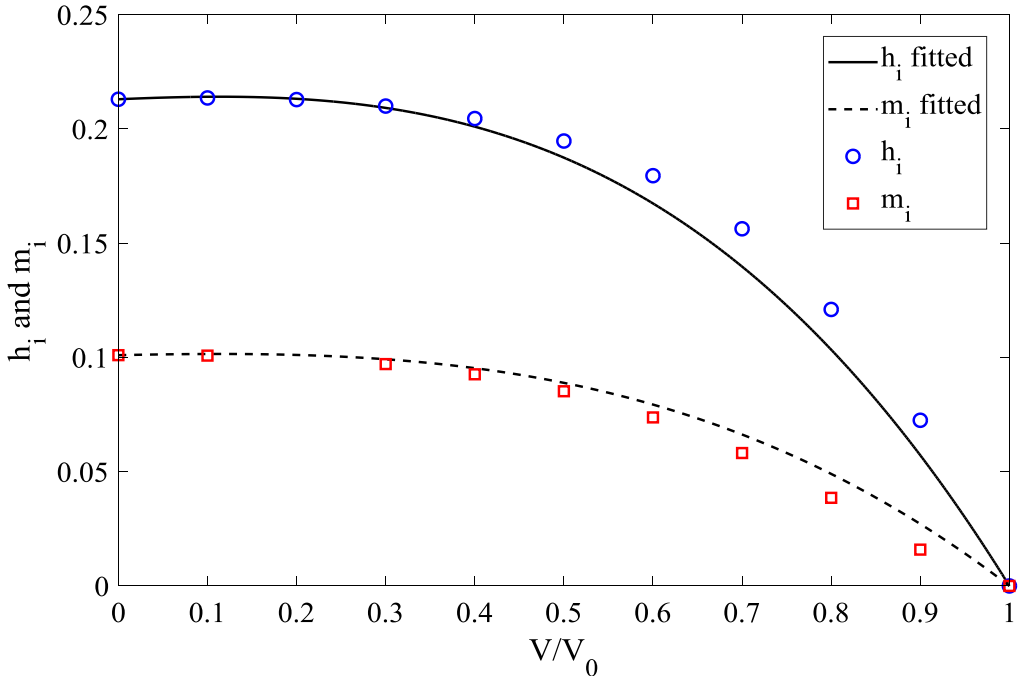
0.25
0.2
0.15
0.1
0.05
0
h_i and m_i
0
0.1
0.2
0.3
0.4
0.5
0.6
0.7
0.8
0.9
1
V/V_0
h_i fitted
m_i fitted
h_i
m_i

(b)

Figure 11

(a) R^2=0.982

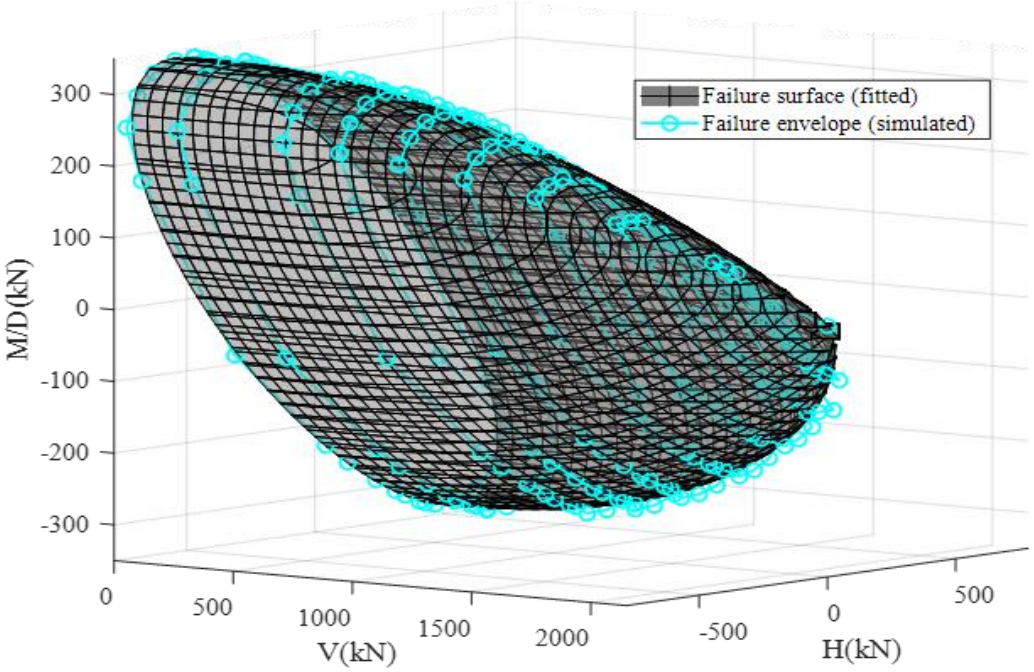

(b) R^2=0.873

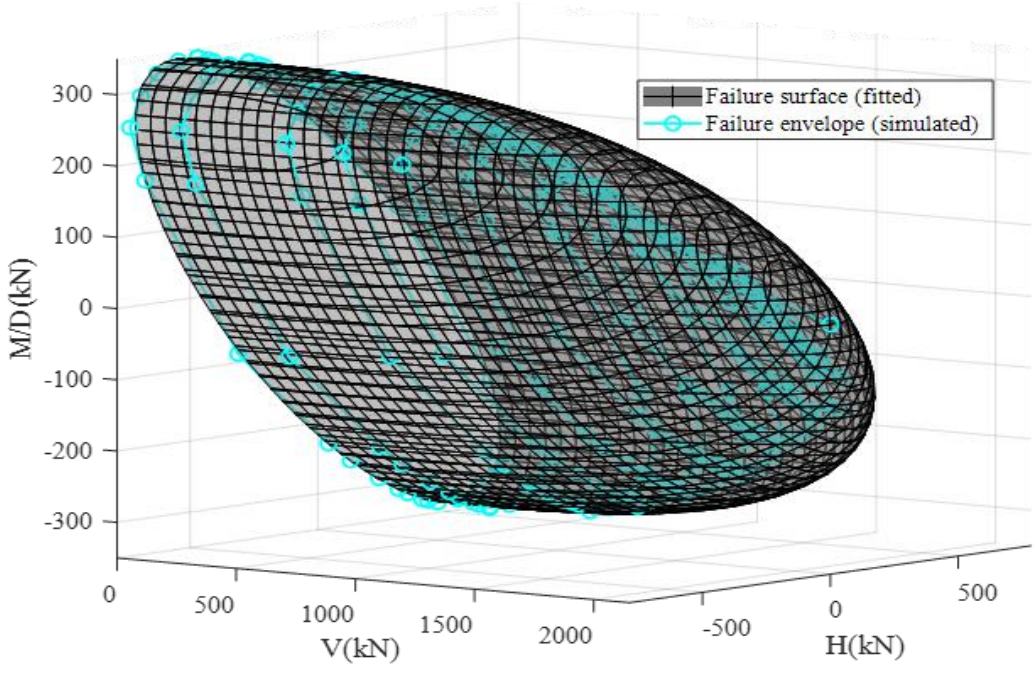

Figure 12

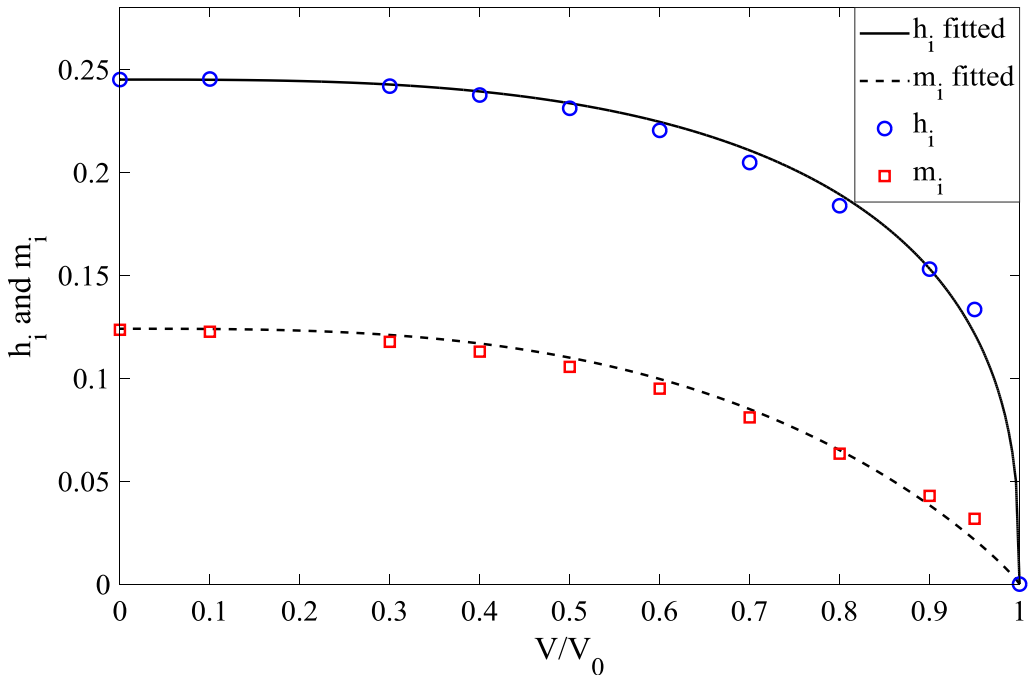

Figure 13

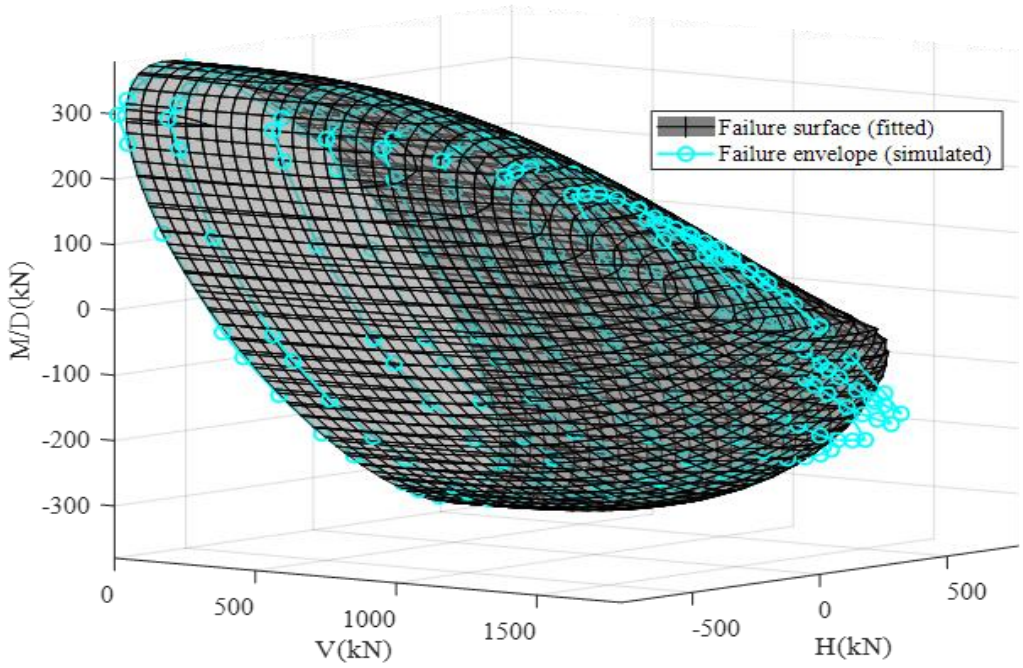

R^2=0.979

Figure 14

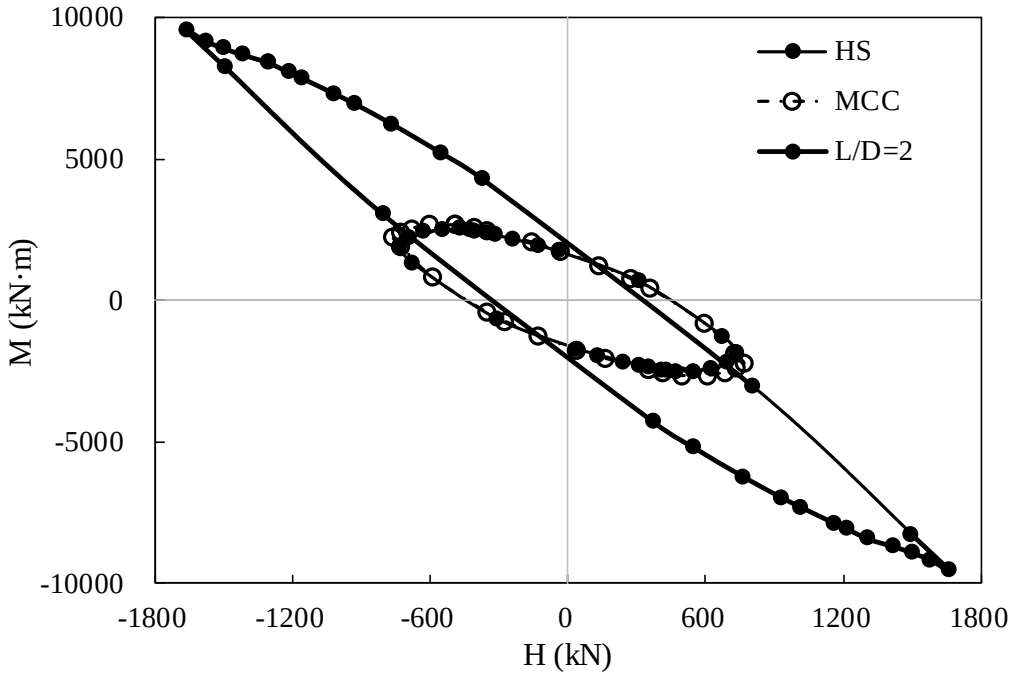
10000
5000
0
-5000
-10000
M (kN·m)
-1800
-1200
-600
0
600
1200
1800
H (kN)
HS
MCC
L/D=2

(a)

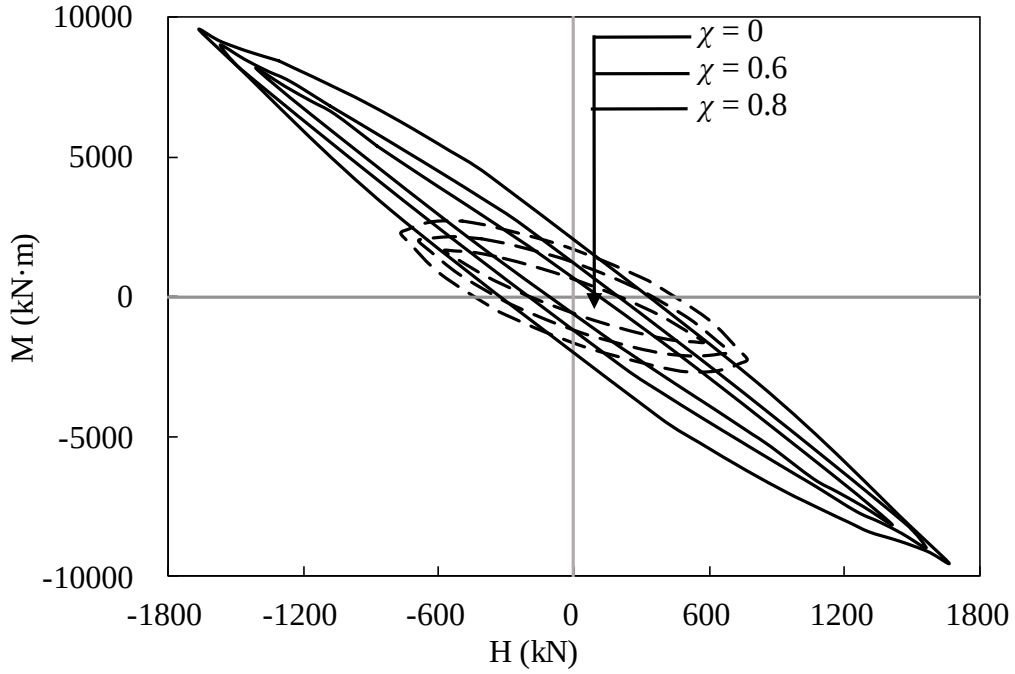
10000
5000
0
-5000
-10000
M (kN·m)
-1800
-1200
-600
0
600
1200
1800
H (kN)
χ = 0
χ = 0.6
χ = 0.8

(b)

Figure 15

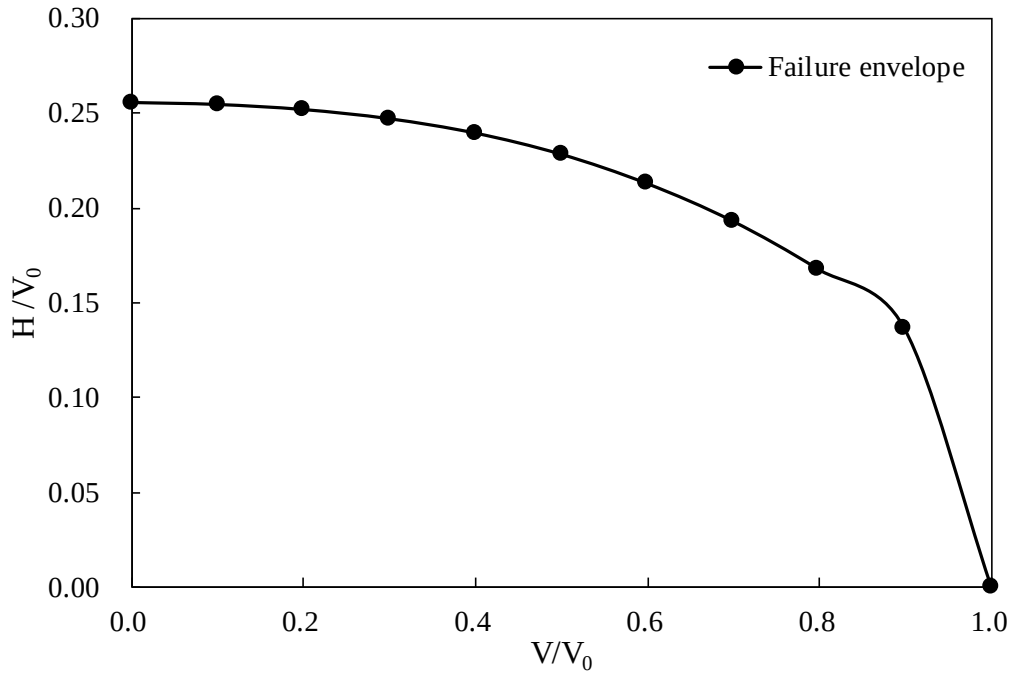

Figure 16

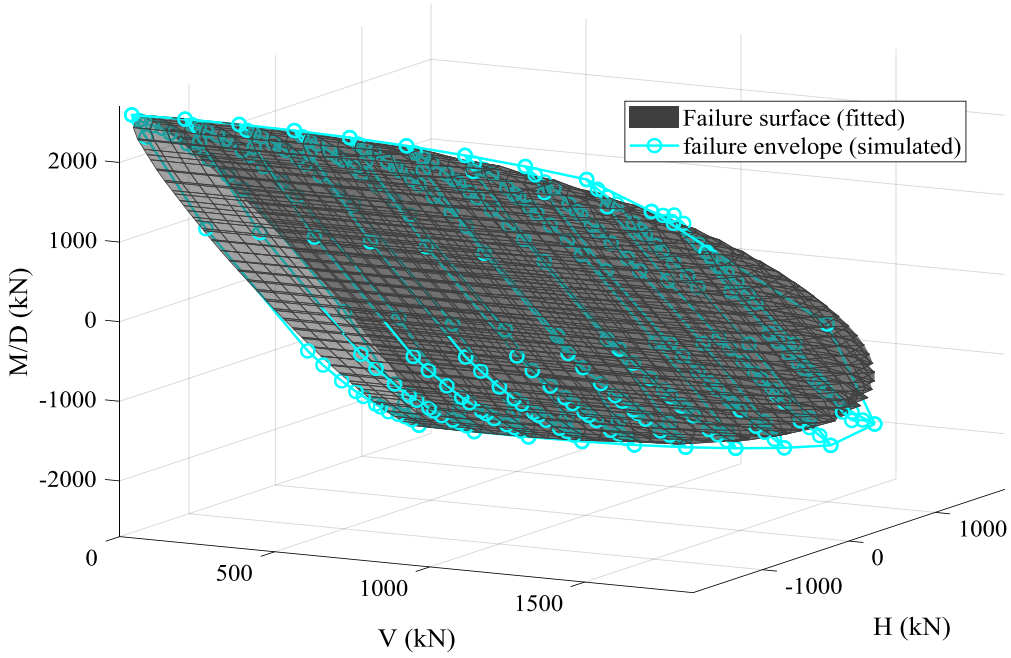

R^2=0.91

Figure 17

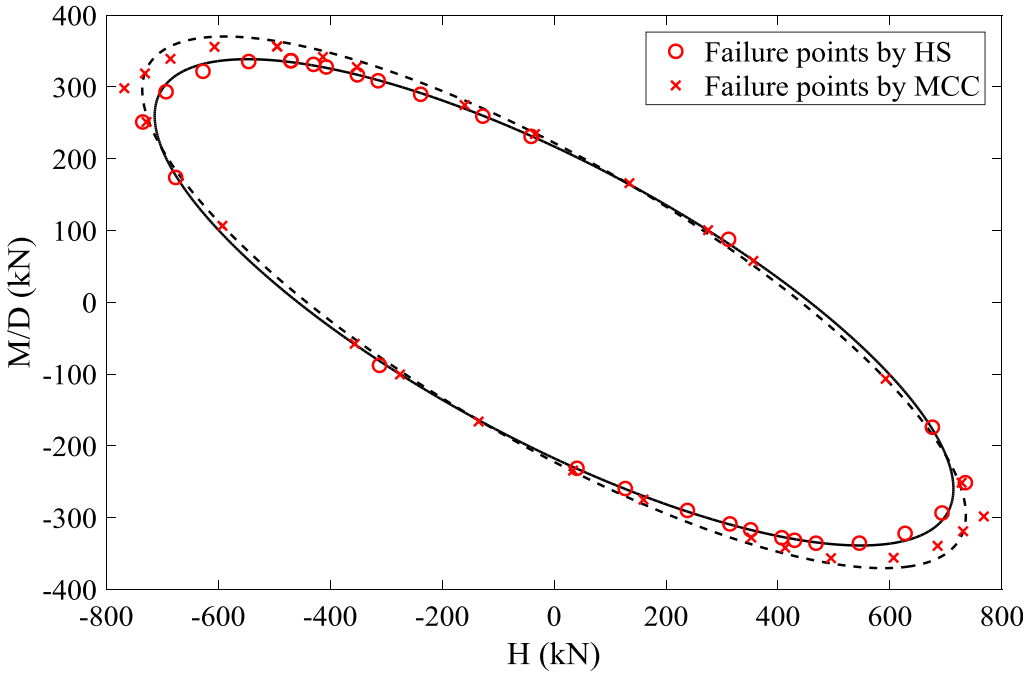

Figure 18

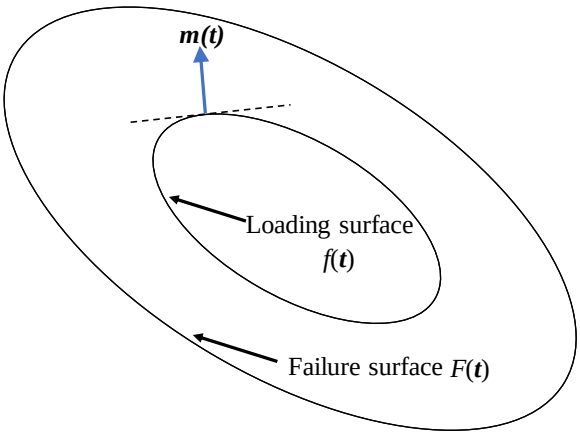

Figure 19

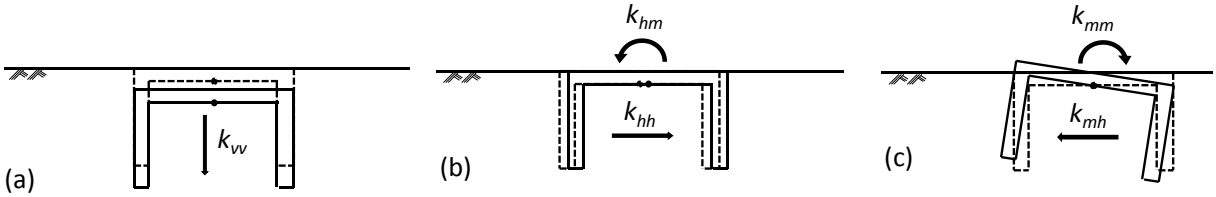

Figure 20

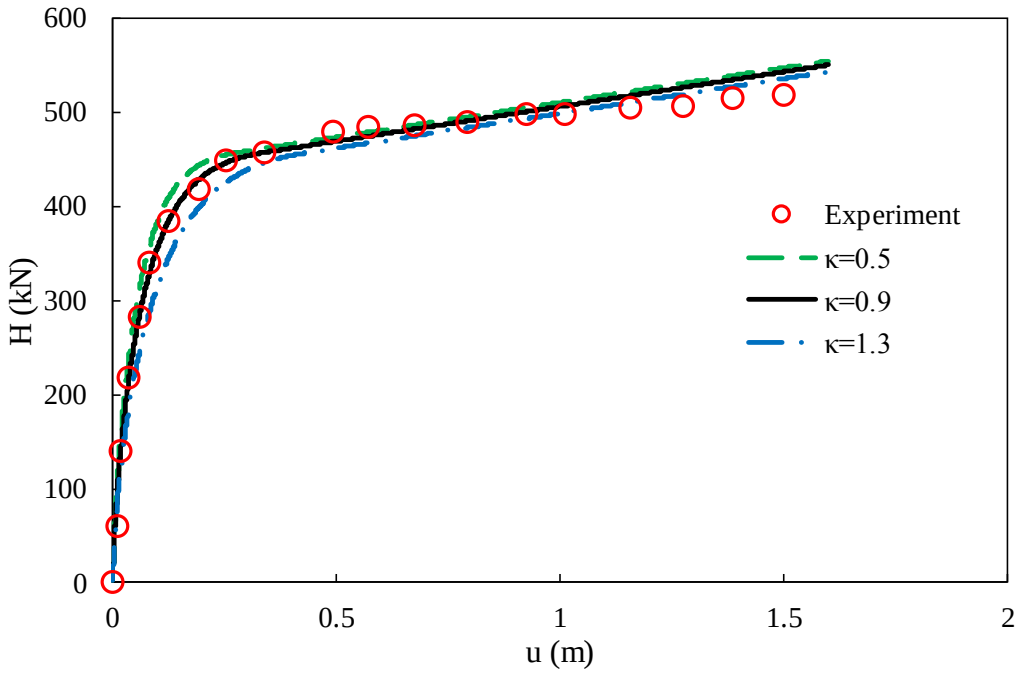
600
500
400
300
200
100
0
H (kN)
0
0.5
1
1.5
2
u (m)
Experiment
κ=0.5
κ=0.9
κ=1.3

(a)

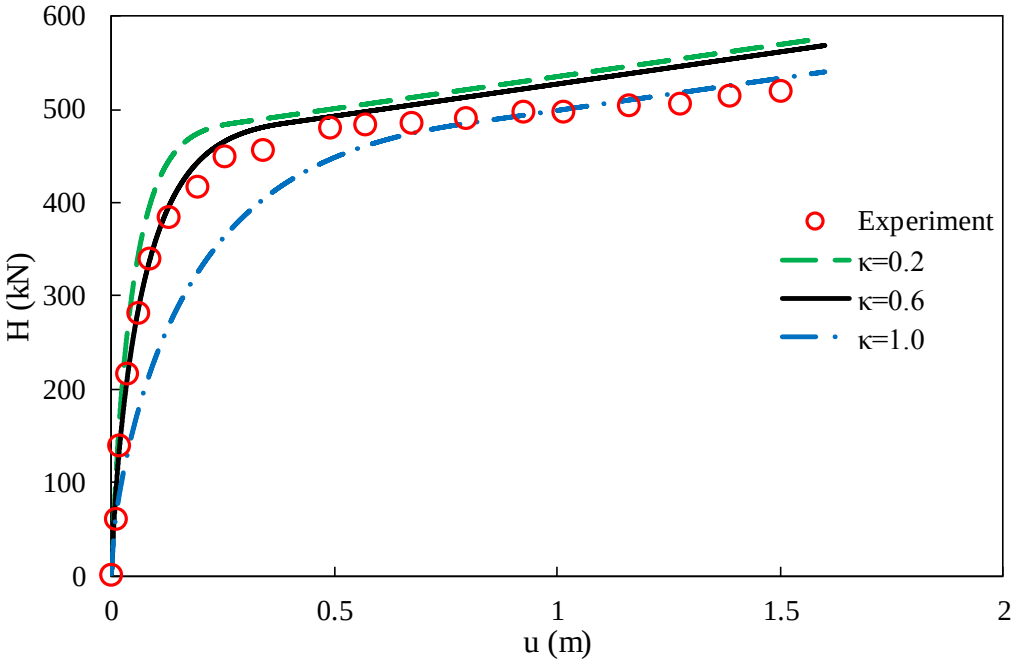
600
500
400
300
200
100
0
H (kN)
0
0.5
1
1.5
2
u (m)
Experiment
κ=0.2
κ=0.6
κ=1.0

(b)

Figure 21

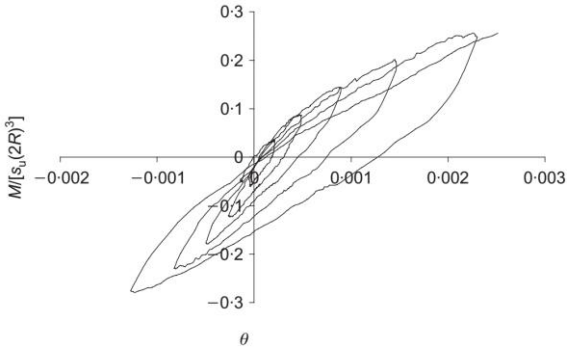

(a) Field test

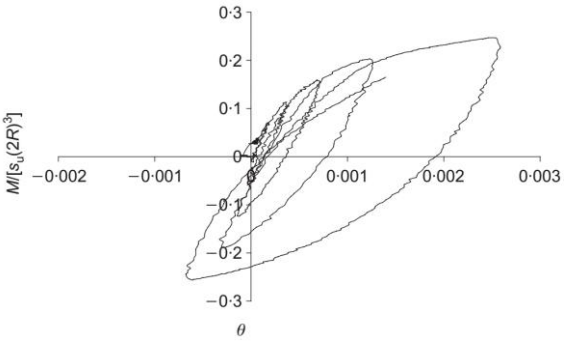

(b) Laboratory test

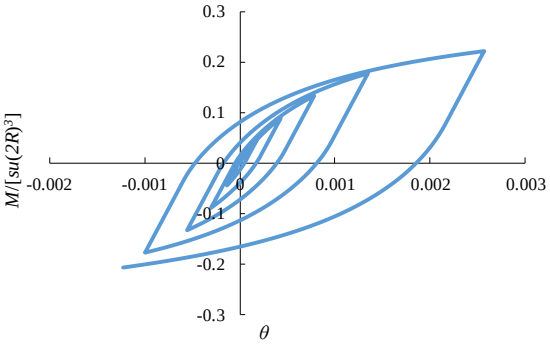

(c) Macro-element based on HS

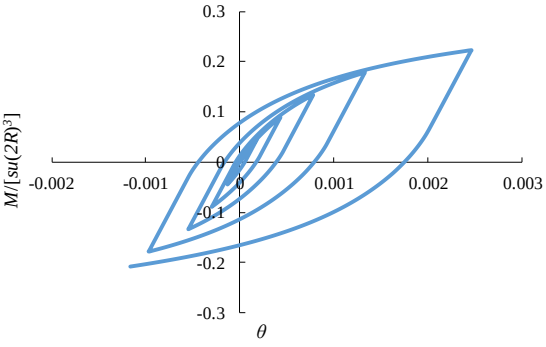

(d) Macro-element based on MCC

Figure 22

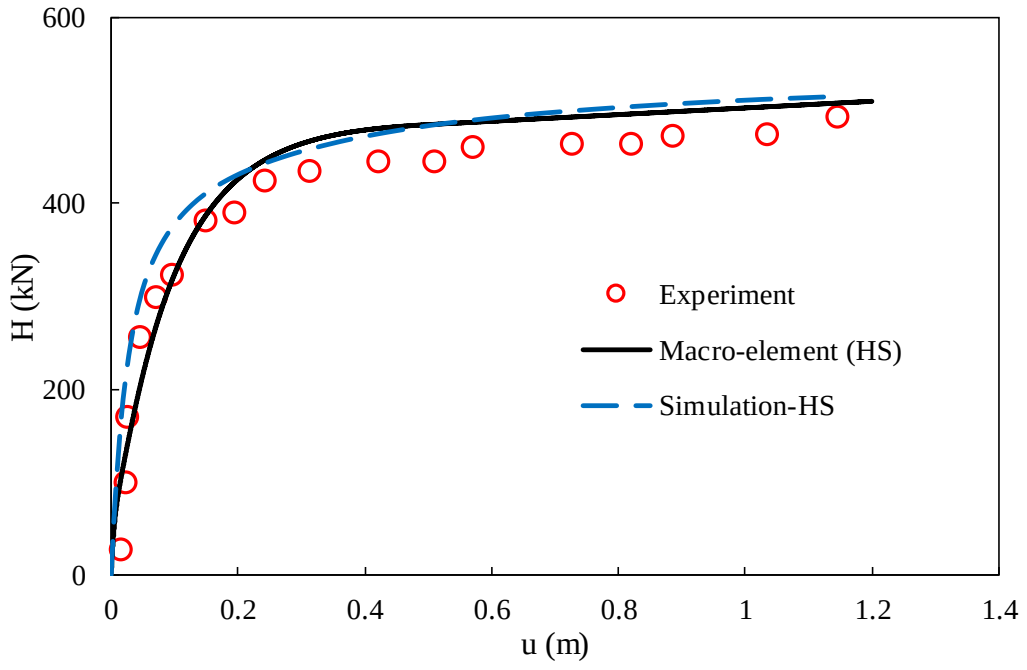
600
400
200
0
H (kN)
0
0.2
0.4
0.6
0.8
1
1.2
1.4
u (m)
Experiment
Macro-element (HS)
Simulation-HS

(a)

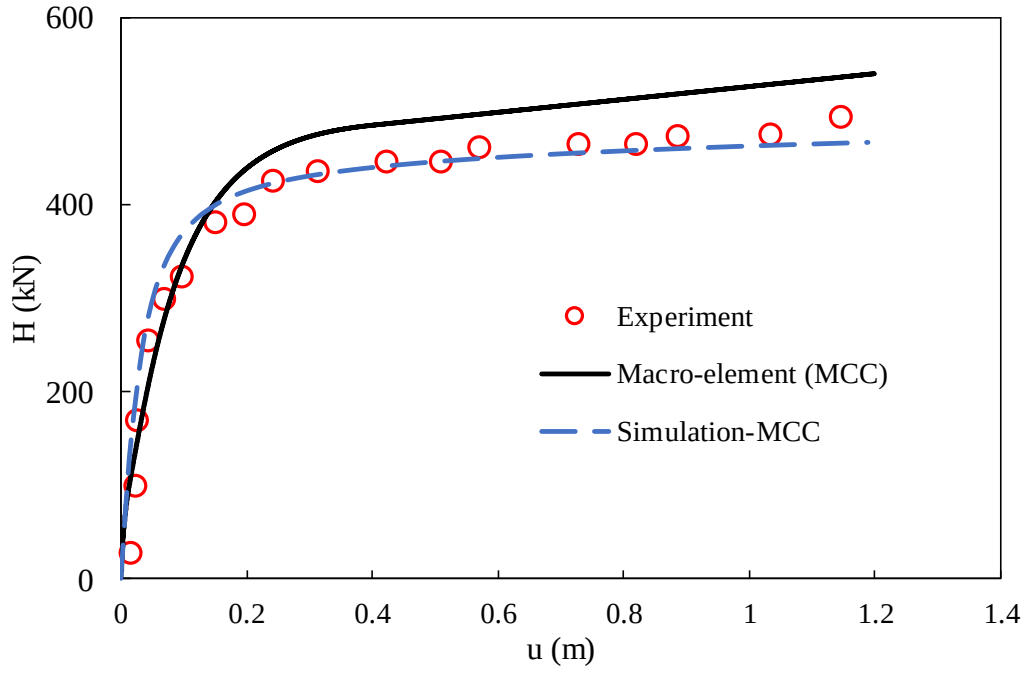
600
400
200
0
H (kN)
0
0.2
0.4
0.6
0.8
1
1.2
1.4
u (m)
Experiment
Macro-element (MCC)
Simulation-MCC

(b)

Figure 23

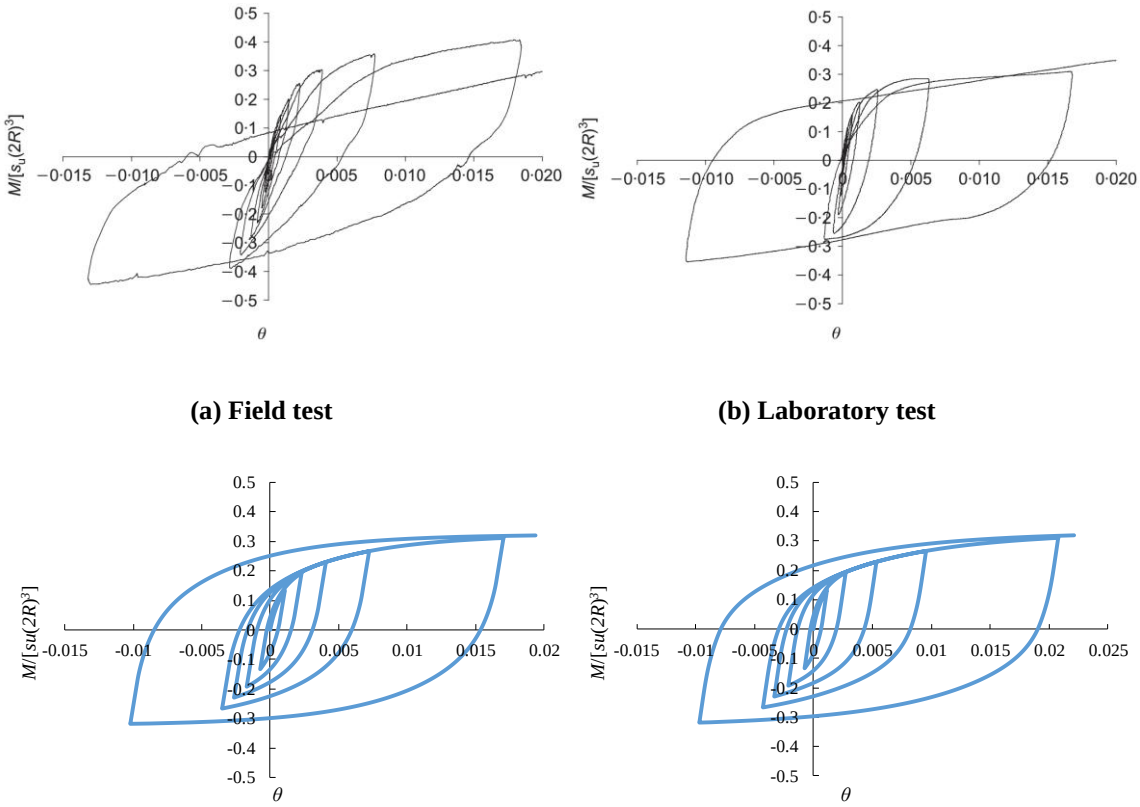

(a) Field test **(b) Laboratory test**

(c) Macro-element based on HS **(d) Macro-element based on MCC**

Figure 24

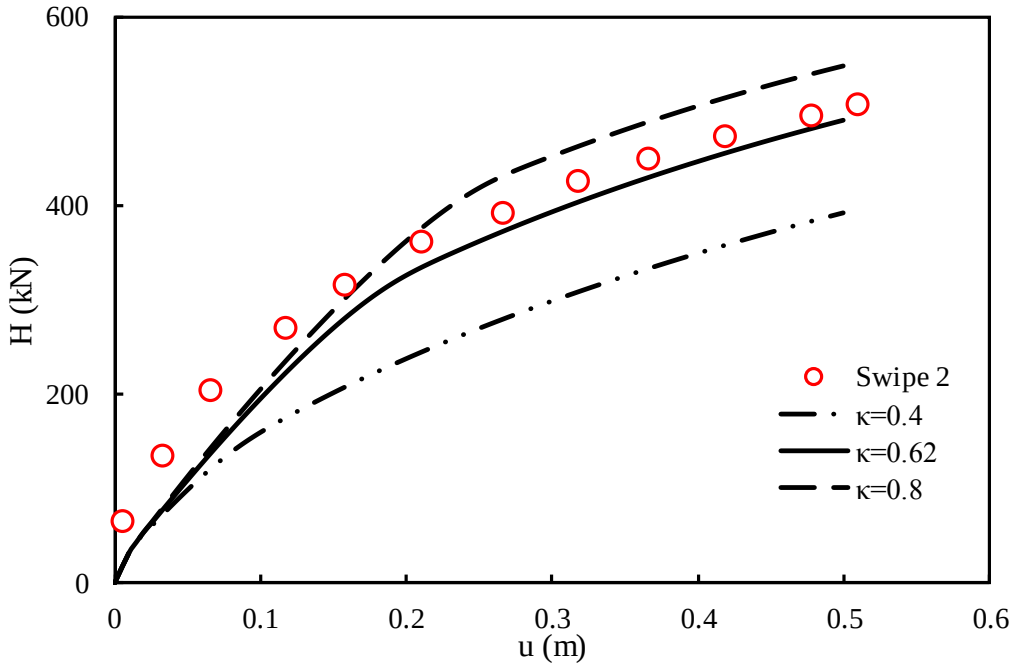

Figure 25